Analyst

Accepted Manuscript

This article can be cited before page numbers have been issued, to do this please use: S. Hatch, J. Nguyen, J. A. Dumouchel, A. Rana and J. E. Dick, *Analyst*, 2026, DOI: 10.1039/D6AN00461J.

View Article Online
DOI: 10.1039/D6AN00461J

Electroanalysis in a Dissolving Microdroplet

Savannah M. Hatch[a, ^], James H. Nguyen[a, ^], Jocelyn A. Dumouchel[a], Ashutosh Rana[a], and Jeffrey E. Dick[a,b]*

[a]Department of Chemistry, Purdue University, West Lafayette, IN 47907, USA

[b]Elmore Family School of Electrical and Computer Engineering, Purdue University, West Lafayette, IN 47907, USA

*To whom correspondence should be addressed: jdick@purdue.edu

Abstract

Electroanalytical chemistry has increasingly focused on probing dynamic, non-equilibrium processes that remain difficult to access using conventional approaches like bulk measurements where the electrolyte and evaporation/dissolution processes are approached as static; recent advances have extended these capabilities to the single-entity level through stochastic electrochemistry. Within this framework, microdroplet-based systems have emerged as powerful platforms for studying confined chemical processes at electrified interfaces, particularly in biphasic environments. Here, we introduce dissolving microdroplet electroanalysis as an emerging approach for interrogating multiphase interfacial dynamics. Unlike conventional assumptions of stability, individual microdroplets confined to electrified microinterfaces do not remain static but continuously dissolve, evolving in size, composition, and interfacial area during measurement. This dynamic evolution directly generates electrochemical signals that encode interfacial transport and reaction processes at liquid-liquid and liquid-solid boundaries. We show that this evolving microenvironment enables intrinsic concentration enrichment and biphasic catalytic amplification, achieving detection down to attomolar concentrations and, in some cases, approaching fewer than 1000 analyte molecules. Beyond sensing, this framework enables quantification of microdroplet lifetimes, extraction of liquid-liquid diffusion coefficients, and access to nanoscale fluctuations associated with dynamic slipping events at the multiphase boundaries. By directly linking microdroplet evolution to electrochemical response, this approach establishes a versatile platform for probing interfacial reactivity, transport, and transient chemical states in evolving volumes and motivates broader adoption for uncovering physicochemical phenomena that remain inaccessible using conventional methods.

Keywords: Stochastic electrochemistry, Microdroplets, Electroanalysis, Single-entity electrochemistry, Sensing

View Article Online
DOI: 10.1039/D6AN00461J

Introduction

The ability to extract physicochemical information from dynamic, non-equilibrium systems represents a defining frontier in analytical chemistry. Scholz suggests that future studies of these systems are critical, and there is a need for experiments on microdroplets that reveal a thermodynamic difference from bulk studies[1]. Electroanalytical methods are uniquely positioned in this space, where transient current and potential responses provide direct access to interfacial processes that are otherwise inaccessible[2–6]. Recent advances have pushed these measurements to the single-entity limit, enabling quantitative insight into the behavior of individual nanoparticles, electrochemical sensing events, confined reaction volumes, and nanodroplet-mediated phenomena[7–19]. Within this framework, stochastic electrochemistry has emerged as a key development, where discrete current transients arising from individual collision or interaction events of micro- and nanoscale entities, such as droplets, nanoparticles, and enzymes, are used to probe single entities in real time[14,16,20]. This approach has enabled unprecedented insight into catalytic activity, reaction kinetics, sensing capabilities, and interfacial dynamics at the nanoscale[2,5,21,22].

Within this broader landscape of single-entity electrochemistry, evolving microdroplet-based systems have emerged as a particularly powerful class of platforms for probing confined chemical processes[23–29]. Significant effort has therefore been dedicated to electrochemical studies of such systems at electrified interfaces, particularly within biphasic emulsion-based environments. These include configurations where an oil microdroplet resides on an electrode immersed in an aqueous phase (and vice versa), as well as emulsions in which droplets stochastically collide with electrode surfaces in bulk media (and vice versa), forming dynamic liquid–liquid interfaces. Foundational contributions from several groups have established microdroplet-based electroanalysis as a rigorous measurement platform and defined how electrochemical signals from confined and stochastic systems are interpreted[30–35]. More recently, analogous concepts have been extended to liquid–air interfaces, further broadening the scope of microdroplet-based electroanalysis[36–42]. Groups such as Alam and co-workers have investigated droplet-based systems as electrically active microreactors for label-free sensing[43–45]. Their work focuses on monitoring electrical properties, such as impedance and capacitance, as droplets evaporate[46,47]. This enables the extraction of information related to ion distribution, biomolecular interactions, and cellular responses[38,45,48]. By leveraging evaporation-driven concentration effects and interfacial charge dynamics, these systems provide a sensitive platform for probing complex chemical and biological processes without relying on Faradaic reactions. Additionally, Anand and co-workers investigate droplet-based systems within microfluidic and electrokinetic platforms, where droplets act as confined environments for biological analysis and manipulation[49–51]. The droplet systems are designed as electrically controlled microreactors for bioanalysis. Phenomena such as ion concentration polarization, electrokinetic enrichment, and dielectrophoresis are manipulated in

View Article Online
DOI: 10.1039/D6AN00461J

droplets for accelerated biochemical reactions[52–54]. Furthermore, Kennedy and coworkers study droplet-based systems through droplet microfluidics coupled with mass spectrometry and electrophoresis[55,56]. By integrating these droplet platforms with sensitive detection methods, it enables rapid, label-free analysis of complex chemical and biological samples with minimal reagent consumption[57,58].

Measurement science is old. Electrochemistry is old. Yet progress in both has relied on pushing limits of detection through confinement, concentration enrichment, and temporal resolution. Stochastic electrochemistry represents a more recent and exciting direction in this evolution. Our group has been working in this space, particularly in emulsion-based systems, to study electrochemical processes in confined volumes[59–65]. At the behest of colleagues, we began exploring a complementary approach that combines microfluidics with electrochemistry, where single microdroplets can be positioned on ultramicroelectrodes (UMEs). The goal was simple: to create a stable, confined microenvironment and probe discrete electrochemical events. However, what we observed challenged this expectation. These droplets did not remain stable. They dissolved. They moved. They evolved with time. This observation, while simple, proved to be critical. It revealed that droplets in biphasic electrochemical systems, often assumed to be quasi-sessile, are in fact continuously evolving entities, with changes in size, composition, and interfacial structure occurring throughout the measurement. Despite decades of work in microdroplet-based electrochemistry, this behavior has largely remained unaccounted for in the interpretation of electrochemical signals. What has been treated as a stable measurement platform is, in reality, an actively changing system.

This perspective consolidates recent contributions of electrochemistry in discrete, actively dissolving microdroplets and establishes a unifying framework for electroanalysis in dynamically evolving volumes. We show that electrochemical measurements, when combined with finite element modeling, directly encode dissolution dynamics, enabling volumes spanning sub-nanoliter to sub-picoliter regimes to be tracked without the need for optical methods[66]. In doing so, electrochemistry transitions from a probe of reactivity to a direct reporter of evolving geometry and interfacial structure. This shift enables capabilities beyond conventional electroanalysis. As the microdroplet dissolves, it inherently preconcentrates confined species, creating a dynamic microenvironment that can be exploited for sensing[67]. We demonstrate detection down to nanomolar concentrations and, when coupled with catalytic amplification strategies, such as EC′ mechanisms and partitioning-driven advantages, sensitivity approaching fewer than 1000 analyte molecules[68]. At the same time, the evolving volume provides an intrinsic timescale, enabling precise quantification of microdroplet lifetimes and extraction of key physicochemical parameters, including liquid–liquid diffusion coefficients[69]. In this way, the same signal that reports on reactivity simultaneously encodes the dynamics of the system. Importantly, this dynamic behavior is directly imprinted in the electrochemical signal. Rather than remaining smooth, current transients exhibit fluctuations during active dissolution that encode stochastic interfacial slipping events at three-phase boundaries on the microdroplets.

View Article Online
DOI: 10.1039/D6AN00461J

These signatures provide access to nanoscale dynamics that are otherwise inaccessible using conventional techniques[70].

More broadly, this Perspective argues that dissolving microdroplets constitute a distinct electroanalytical regime in which interfacial transport, reaction kinetics, confinement, and phase evolution are intrinsically coupled rather than independently controlled. In this framework, the evolving droplet is not merely a passive reaction vessel, but an active component of the measurement itself, where temporal changes in geometry and composition directly generate experimentally accessible electrochemical information. By framing droplet dissolution as an electroanalytically useful phenomenon rather than an experimental complication, this approach establishes connections between stochastic electrochemistry, confined-volume analysis, interfacial transport, and non-equilibrium chemical systems.

Taken together, these results show that droplets in such systems cannot be treated as static microreactors. Instead, actively dissolving droplets define a measurement regime in which reaction, transport, and phase evolution are intrinsically coupled. This perspective presents electroanalysis in such systems as a versatile and general platform for probing interfacial reactivity, transport processes, and transient chemical states within dynamically evolving volumes. More broadly, we aim to motivate wider adoption of this platform, as it opens new avenues for uncovering physicochemical properties and interfacial phenomena that remain difficult to access using conventional approaches.

Measuring Physicochemical Properties of Dissolving Microdroplets

View Article Online
DOI: 10.1039/D6AN00461J

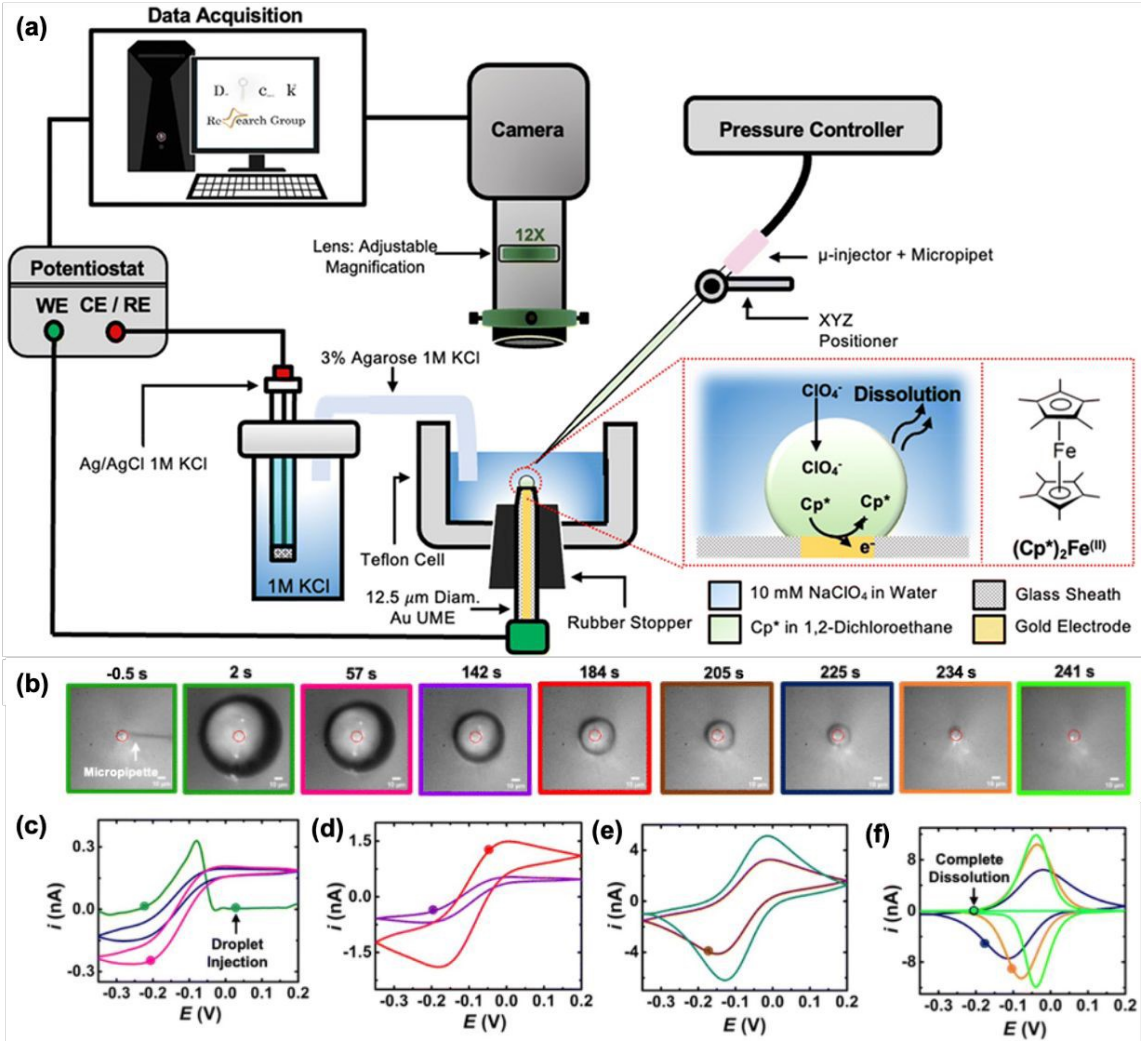

Figure 1. (A) Cross sectional schematic of the setup used to visualize microdroplet dissolution while simultaneously recording their electrochemical response. A 6.3 μm radius gold microelectrode is held vertically in a Teflon cell (grey color) containing about 3 mL of 10 mM $NaClO_4$ aqueous solution (light blue color). The gold micro disk is imaged with the camera positioned above the cell. The microinjection system is used to deliver about $(Cp^*)_2Fe^{II}$ in DCE just on top of the gold micro disk. The resulting DCE microdroplet is shown in green on the scheme. The electrochemical response is measured in a two-electrode configuration with an Ag/AgCl in 1 M KCl reference/counter electrode placed in a separate container and connected to the Teflon cell *via* a salt bridge. The chemical structure of the reduced form of redox molecule, $(Cp^*)_2Fe^{II}$, is provided on the right. Charge balance inside the microdroplet is maintained by the transfer of ClO_4^- across the water|DCE interface. (B) Top-view optical micrographs of a dissolving 51 μm radius droplet containing 155 μM of $(Cp^*)_2Fe^{II}$ in a 10 mM $NaClO_4$ aqueous bulk phase. The solid red line incrusted in the micrographs indicates the position of the gold-disk electrode. The scale bar is 10 μm. Panels (C)–(F) show cyclic voltammograms recorded simultaneously with the optical micrographs during the dissolution of the DCE droplet at a scan rate of 0.2 V s^{-1}. The points on the cyclic voltammogram indicate the exact time when the frames in (A) were taken. Figure modified with permission from reference[66].

View Article Online
DOI: 10.1039/D6AN00461J

We used 1,2-dichloroethane (DCE) as the solvent for microdroplet analysis in an aqueous system, entering the experiment with a preconception that the organic microdroplet was fully immiscible with water when we discovered, to our dismay, that DCE microdroplets slowly dissolve into an aqueous bulk. We did not realize, in that moment, that this accidental discovery would spark an entirely new area of electroanalytical chemistry, allowing us to extract physical coefficients, precisely measure microdroplet lifetimes, and unlock a concentration enrichment effect that can probe less than 1,000 molecules in solution.

Figure 1 shows the evolution of our experimental process: as the microdroplet dissolved into the aqueous bulk, we found that it is possible to probe the system electrochemically by dispersing the microdroplet onto an ultramicroelectrode (Fig. 1F). This methodology provides valuable insight into the dynamics of a dissolving droplet, reflected in the changing cyclic voltammogram (Fig. 1B-E). To preface our discussion of this system, we first present the physical parameters that facilitate droplet dissolution.

Physical Parameters Governing Droplets: Kinetics of Microdroplet Shrinkage

Microdroplets have emerged in recent decades as an experimental system characterized by accelerated reaction mechanisms and the spontaneous undertaking of thermodynamically unfavorable reactions. Microdroplets exhibit distinctive properties that enable thermodynamically and kinetically improbable reactions to occur without the intensive manipulation that is typically required for the same reaction in bulk phases.

One of the key features that distinguish microdroplets from bulk systems is the high surface area to volume ratio. A large surface area increases the relative amount of analyte that is near the oil|water interface, where one sees accelerated reaction kinetics. Reactions proceed faster at the oil|water interface due to partial solvation and its impacts, such as stabilization of intermediates and lowering of interfacial tension[71]. These effects result in reduced energy barriers, increased concentration of analytes, and reactions that are 20x more efficient, or in the case of enzymatic activity, two orders of magnitude greater[72].

An additional advantageous feature of microdroplets is surface charge. Both naturally occurring, such as atmospheric water droplets, and experimentally produced, like droplets generated from electrospray ionization, carry charge and have electric fields[72]. This intrinsic charge has been harnessed by many researchers for a variety of experiments; for example, Banerjee's group used this to isolate and analyze unstable carbocations[72]. In this case, they used positively charged water microdroplets to function as an electron-donating group for carbocation stability. If an aliquot is bombarded with positively charged water droplets, these droplets will pick up and trap carbocation intermediates for analysis using mass spectrometry[72]. Charged microdroplets can also be used to accelerate redox reactions where they function as an electron source or sink. In a controlled or natural cloud of droplets, both positively and negatively charged droplets can be measured; these opposite microdroplet charges can oxidize and reduce, a distinctive feature of cloud

View Article Online
DOI: 10.1039/D6AN00461J

electrochemistry[39,73]. Additionally, at the gas|aqueous interface, oxygen and nitrogen species can facilitate a vast array of chemical transformations, such as redox, addition, condensation, reductive amination, decarboxylate coupling, and radical reactions[74].

The physicochemical properties of microdroplets are directly responsible for the distinct mechanisms observed in these experiments. Pairing microdroplets with electroanalytical techniques, such as chronoamperometry and cyclic voltammetry, can provide mechanistic insight into microdroplet properties, like dissolution kinetics, microdroplet lifespan, and movement behavior. This section will explore electrochemistry to observe and analyze microdroplet behavior.

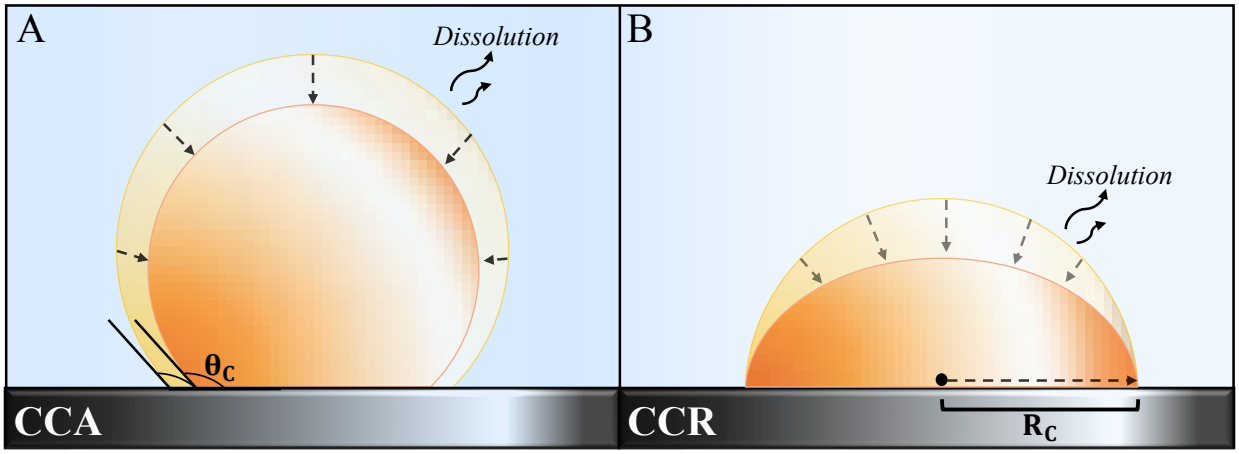

Figure 2. Schematic depicting various modes of microdroplet dissolution: Constant Contact Angle Mode (CCA) and Constant Contact Radius Mode (CCR).

When studying microdroplet dissolution, it is important to understand the governing mechanics of this process. Much like a microdroplet evaporating in air, the dissolution of a microdroplet in liquid is controlled by the principles of diffusion. There are two main modes of microdroplet dissolution that are widely agreed upon: constant contact angle (CCA) mode and constant contact radius (CCR) mode[66,75]. In CCA mode, the contact angle of the microdroplet to the surface will remain constant as the radius of the microdroplet decreases (Fig. 2A). In CCR mode, the radius of the microdroplet will remain fixed as the contact angle decreases (Fig. 2B). These two modes are often combined in a variety of ways, leading to what is referred to as "mixed modes" of dissolution. One of these is the stick-jump mode, where a microdroplet will dissolve in CCR mode with intermittent jumps to a new contact angle and microdroplet radius[76]. The stick-jump mode of dissolution occurs most often in droplets that contain a significant number of large particles. Another mixed mode is the zipping-depinning mode, which can be observed on droplets adsorbed to a surface with microring grooves[77]. A final mixed mode is the slip-stick mode, where a microdroplet will shrink in CCR mode until the triple-phase boundary becomes pinned, after which the dissolution mode will change to CCA mode[66]. Throughout the entire dissolution process of a microdroplet, surface tension is a stronger influence than gravitational forces, ensuring that the microdroplet retains spherical geometry.

View Article Online
DOI: 10.1039/D6AN00461J

The two dissolution modes, CCA and CCR, are commonly measured using contact angle goniometry; a technique that involves pipetting a droplet onto a hydrophobic or hydrophilic substrate and monitoring the contact angle evolution from a side-profile with a high-resolution camera[75,78,79]. The droplet dissolution can be observed until it can no longer be resolved by the camera (<0.01 μL)[78]. For our experiments, a top-down profile was used for imaging (Fig. 1B), and the dissolution mode could not be ascertained optically. For this reason, finite element models were simulated on COMSOL Multiphysics® software, and the microdroplet dissolution mode(s) was investigated by comparing simulated CV responses with experimental results (Fig. 3)[66].

View Article Online
DOI: 10.1039/D6AN00461J

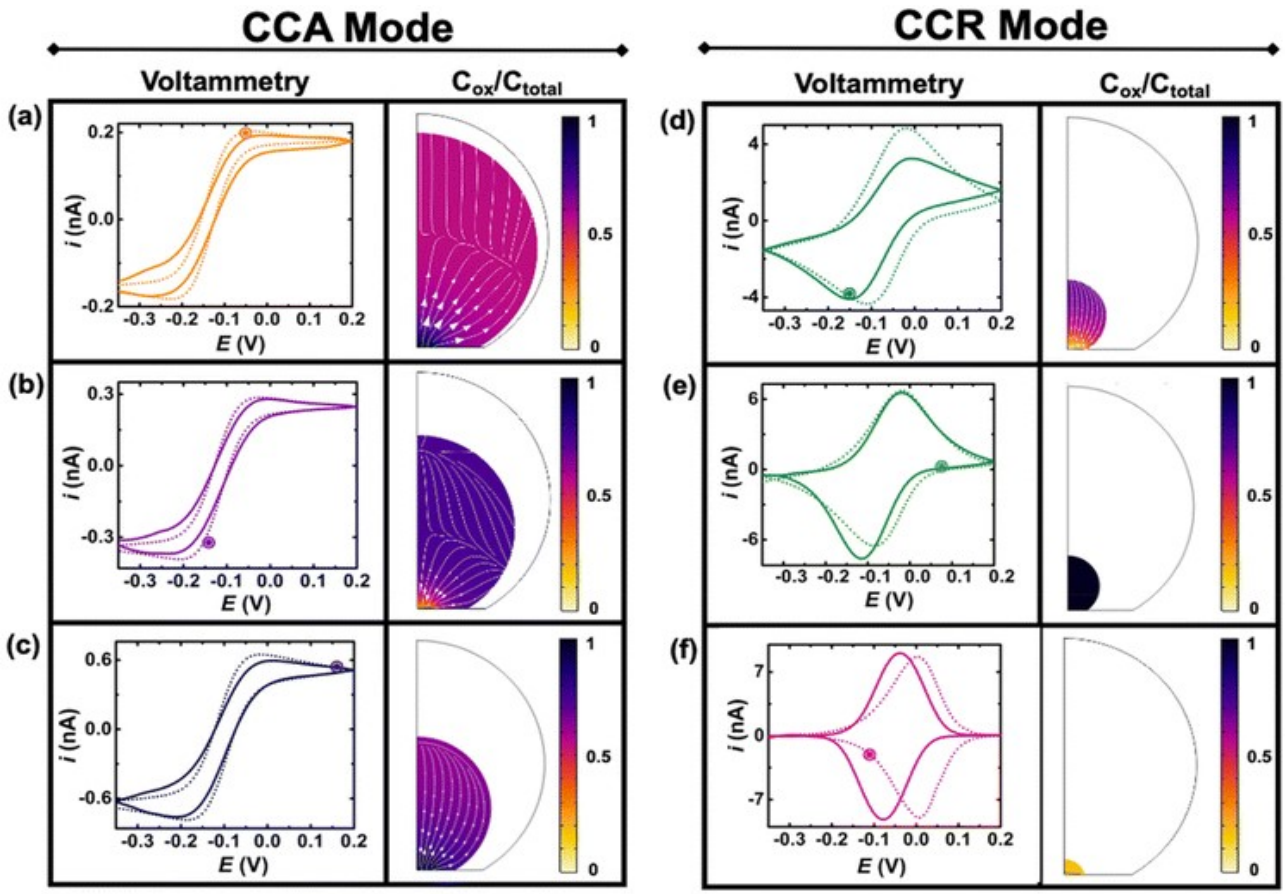

Figure 3. Comparison of experimental (continuous lines) and simulated (dashed lines) cyclic voltammograms during the dissolution of a DCE droplet. The color profiles represent the ratio $[(Cp^*)_2 Fe^{III}]/([(Cp^*)_2 Fe^{II}] + [(Cp^*)_2 Fe^{III}])$, which is denoted as C_{ox}/C_{tot} for the sake of clarity. The arrows describe the flux of $(Cp^*)_2Fe^{III}$. The concentration profiles and fluxes are taken at the time indicated by a circle on the voltammogram. The panels (A), (B), (C), (D), (E) and (F) correspond to the 6th (t = 29 s, C_{total} = 0.197 mM), 17th (t = 92 s, C_{total} = 0.373 mM), 26th (t = 139 s, C_{total} = 0.719 mM), 38th (t = 208 s, C_{total} = 4.76 mM), 41st (t = 223 s, C_{total} = 8.22 mM), and 43rd (t = 235 s, C_{total} = 98 mM) cyclic voltammogram, respectively. The parameters of the simulation are as follows: initial concentration of redox couple (155 µM), initial ox/red ratio (20/80), diffusion coefficients of $(Cp^*)_2Fe^{II}$ and $(Cp^*)_2Fe^{III}$ in DCE (8.8×10^{-6} and 5.3×10^{-6} cm^2 s^{-1} respectively), radius of electrode (6.3 µm), standard apparent potential (−0.04 V vs Ag/AgCl), standard rate constant for electron transfer (k_0 = 0.01 m s^{-1}), symmetry coefficient (α = 0.5), and the first order rate of loss for $(Cp^*)_2Fe^{III}$ and $(Cp^*)_2Fe^{II}$ (1.20×10^{-6} cm s^{-1} and 0.08×10^{-6} cm s^{-1} respectively). The initial serial resistance is set at 0.1 gigaohm. The transition from CCA to CCR mode is set for a contact radius of 8 µm near the gold|glass interface. Figure taken from reference[66] with permission.

The simulated results suggested that the 1,2-dichloroethane (DCE) microdroplet would shrink in CCA mode until its contact point reached the glass/gold junction of the UME, where it would become pinned due to the surface discontinuity. After this point, the microdroplet dissolves in the aqueous bulk in CCR mode until it reaches thin layer conditions (slip-stick mode).

It is important to note that the reality of dissolving microdroplet kinetics is significantly more complex than two discrete modes, but this approximation remains physically reasonable until the last stages of the CCR phase. Throughout COMSOL simulation measurements, an active deformation mesh was used that captured both CCA and CCR modes. This enabled experimentally

View Article Online
DOI: 10.1039/D6AN00461J

relevant results that further confirmed the proposed slip-stick model. For our model, Popov's dissolution equations were used. Additionally, the concentration of analyte within the microdroplet is approached uniformly; although this is acceptable for macroscopic systems, at this scale the concentration may differ at the liquid|liquid interface due to the coffee-ring effect. This effect can be observed in droplets that are pinned to the triple-phase boundary due to surface roughness[80]. Despite this, the simulated results were sufficient for approximating the dissolution mode that occurred throughout experimentation (Fig. 3).

The geometry simulated experimental conditions by using the experimentally measured radius of the microdroplet as well as theoretical dissolution rate equations. The simulated model validated reproducible experimental results and accurately reproduced the transition in cyclic voltammogram (CV) profiles from sigmoidal to duck shaped as microdroplet volume decreases (Fig. 3). Figure 3 illustrates this effect; the simulation was set to transition from CCA mode to CCR mode when the microdroplet radius reaches 8 μm. Panels A-C of Fig. 3 show that $(Cp^*)_2Fe^{III}$ grows intensely concentrated as the microdroplet size diminishes, and the CV's sigmoidal response begins to widen. Once the microdroplet radius reaches the threshold of 8 μm, the mode changes to CCR and duck-shaped CV responses can be seen, matching experimental observations (Fig. 3D-F).

The utility of finite element modeling lies in its ability to provide quantitative insights that are difficult to gather experimentally. COMSOL simulations provide otherwise unattainable data like the droplets exact volume, concentration of redox analyte, and flux patterns. The model retains accuracy until the microdroplet reaches sub-picoliter volumes, whereafter deviations from reality are seen, likely because the simple CCR model of dissolution insufficiently represents microdroplet kinetics.

Electrochemically Measuring Microdroplet Lifespan

View Article Online
DOI: 10.1039/D6AN00461J

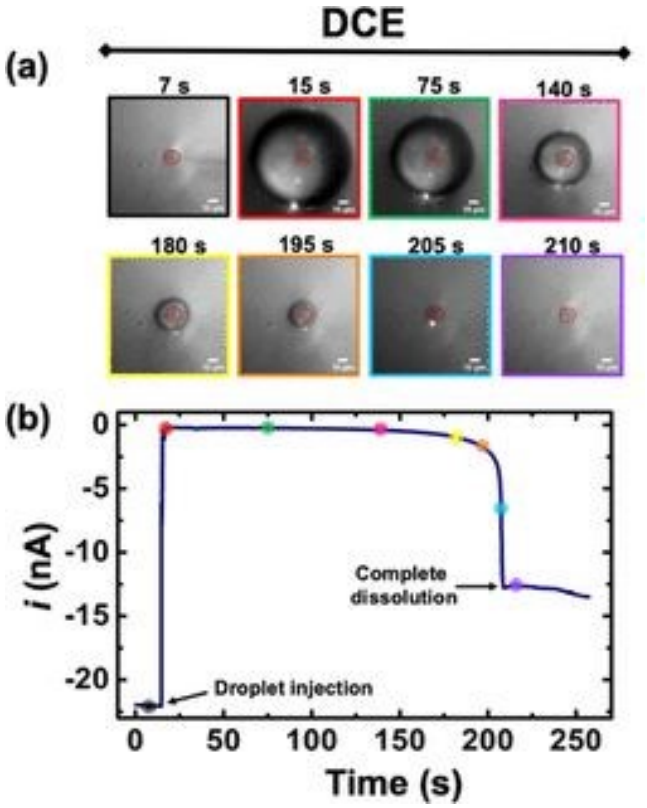

Figure 4. (A) Optical micrographs recorded during the dissolution of a 49 ± 3 µm radius DCE droplet in the aqueous bulk phase. The solid red line in the micrographs indicate the position of the Au disk. The scale bar is 10 µm. (B) i–t response to an applied potential of 0 V vs Ag/AgCl, simultaneously with the optical micrographs during the dissolution of the DCE droplet. The i–t response is color-coded and matches the color code in (A), and the colored points on the i–t response denote the time at which the micrographs in (A) were recorded. Figure adapted from reference[69] with permission.

Traditional methods of monitoring microdroplet lifetimes include atomic force microscopy, dynamic light scattering, and optical microscopy; however, these techniques suffer from various drawbacks like cost, operation complexity, the diffraction limit, temporal capabilities, and versatility[69]. We found that the microdroplet lifespan can simply be measured electrochemically by adding an electroactive reagent to the bulk and using the microdroplet as an insulator[81].

The experimental setup consisted of an aqueous bulk phase containing a redox species that is highly insoluble in organic solvents, like potassium ferricyanide ($K_3[Fe(CN)_6]$) and potassium ferrocyanide ($K_4[Fe(CN)_6]$) with the supporting electrolyte 1 M potassium chloride (KCl). A DCE microdroplet was deposited onto an Au UME using a microinjector. The organic microdroplet acts as an insulator, effectively blocking the redox reaction from contacting the UME (Fig. 4A). On an amperometric i-t curve, the deposition of the microdroplet will manifest as a sharp decrease in current with almost no signal. This is indicative that the redox reaction can no longer contact the electrode surface, and the microdroplet is covering the entirety of the gold disk (Fig. 4B).

We used both $K_3[Fe(CN)_6]$ and $K_4[Fe(CN)_6]$ in the aqueous bulk for a few reasons; first, initial measurements of droplet lifetime were done using cyclic voltammograms and we wanted to keep

View Article Online
DOI: 10.1039/D6AN00461J

experimental conditions consistent throughout different measurements. Additionally, we wanted to ensure that the reagent used during i-t measurements did not influence the microdroplet lifetime measurement. For this reason, we included both $K_3[Fe(CN)_6]$ and $K_4[Fe(CN)_6]$ in the DCE microdroplet and ran two different i-t experiments. First, we held the potential at 0 V vs Ag/AgCl to sufficiently reduce $K_3[Fe(CN)_6]$ to $K_4[Fe(CN)_6]$ while the droplet dissolved (Fig. 4). Next, we repeated the experiment while holding a potential of 0.5 V vs Ag/AgCl to sufficiently oxidize $K_4[Fe(CN)_6]$ to $K_3[Fe(CN)_6]$[69]. We found that if the initial microdroplet size was comparable, the reagent used was irrelevant. For this reason, in future studies we elected to only use $K_3[Fe(CN)_6]$.

The microdroplet slowly dissolves into the aqueous phase, re-exposing the electrode surface to $K_3[Fe(CN)_6]$ and $K_4[Fe(CN)_6]$ (Fig. 4A). An increase in current will appear on the i-t curve, and current will exponentially increase until the microdroplet is fully dissolved (Fig. 4B). Complete dissolution is achieved when exponential growth stops and a new steady-state current is reached. Although the steady-state current fails to return to its original steady-state current for reasons not yet fully understood, ~~one plausible explanation is partial blockage of the electrode surface from an insoluble precipitate~~, the measured diffusion coefficient value for DCE was still comparable to literature. Described in more detail in the next section, the experimental diffusion coefficient value for DCE in water was 9.9 x 10^{-6} cm^2/s and the literature diffusion coefficient value was 1.1 x 10^{-5} cm^2/s[82]. There are a few plausible explanations for this such as adsorption to the electrode from side reactions, accumulation of organic residues from the DCE droplet, or insoluble precipitants that would explain the partial blockage of the electrode surface. Future studies employing surface interrogation techniques could rule out plausible mechanisms that underly the shifted steady-state current post-measurement.

The exact lifespan of the microdroplet can therefore be ascertained by subtracting the time of initial current decrease (microdroplet deposition) from the time where a new steady-state current is achieved (complete dissolution). Figure 4 depicts experimental chronoamperometry data, and microdroplet deposition can be seen in grey before the subsequent current surge towards zero. This is followed by an exponential growth in current, until a new steady-state current is achieved, marked in purple.

Extracting Diffusion Coefficients from Microdroplet Lifespan

Dissolving microdroplet electroanalytical techniques can also be used as an innovative way to measure liquid-into-liquid diffusion coefficients. Currently, dynamic light scattering and fluorescent correlation spectroscopy are common methods to find the diffusion coefficients of particles or molecules; however, these two methods indirectly measure the diffusion coefficient and require expensive and calibrated instrumentation[83]. Electrochemical analysis can determine the lifetime of an organic microdroplet in aqueous bulk solution, and the diffusion coefficient can then be quantified.

View Article Online
DOI: 10.1039/D6AN00461J

From microdroplet lifespan and initial microdroplet size, which can easily be determined with an optical camera, the dissolution coefficient can be determined. For instance, during one experimental trial, using the reaction system detailed above with an initial microdroplet radius of 43 μm, a microdroplet lifespan of 201 s was experimentally measured. This time was used to calculate an experimental diffusion coefficient value for DCE in water of 9.9 x 10^{-6} cm^2/s, which is comparable to the literature diffusion coefficient value 1.1 x 10^{-5} cm^2/s[82]. This calculation was performed using Eq. 1, where τ_{total} is the microdroplet lifespan, D is the diffusion coefficient, and P is a numerically evaluated factor that is dependent on the contact angle and contact radius, determined using MATLAB. Full derivations and explanations of this equation can be found in the supplementary information of reference[69].

$$\tau_{total} = (1/D) \cdot P(\theta_c , R_c(t=0)) \qquad \text{(Equation 1)}$$

It should be noted that varying the initial radii of the DCE droplets should still produce a consistent diffusion coefficient under diffusion-limited conditions[84,85]. Larger droplets exhibit a longer lifespan, whereas smaller droplets dissolve more rapidly due to their high surface-to-volume ratios, which is accounted for in Eq. 1. This behavior is expected provided that: (1) additional mass transfer effects such as Marangoni convection, buoyancy-driven convection, or curvature-dependent effects are negligible; (2) contact angle evolution through CCA and CCR modes remains consistent across microdroplets; and (3) substrate interactions do not significantly perturb droplet dissolution dynamics[84–86].

Experiments were also performed with nitrobenzene as the organic microdroplet, and diffusion coefficients calculated from these results aligned with literature values, indicating that this technique holds broadly for semi-miscible organic droplets in an aqueous bulk.

Detecting Nanoscale Movement of Microdroplets

View Article Online
DOI: 10.1039/D6AN00461J

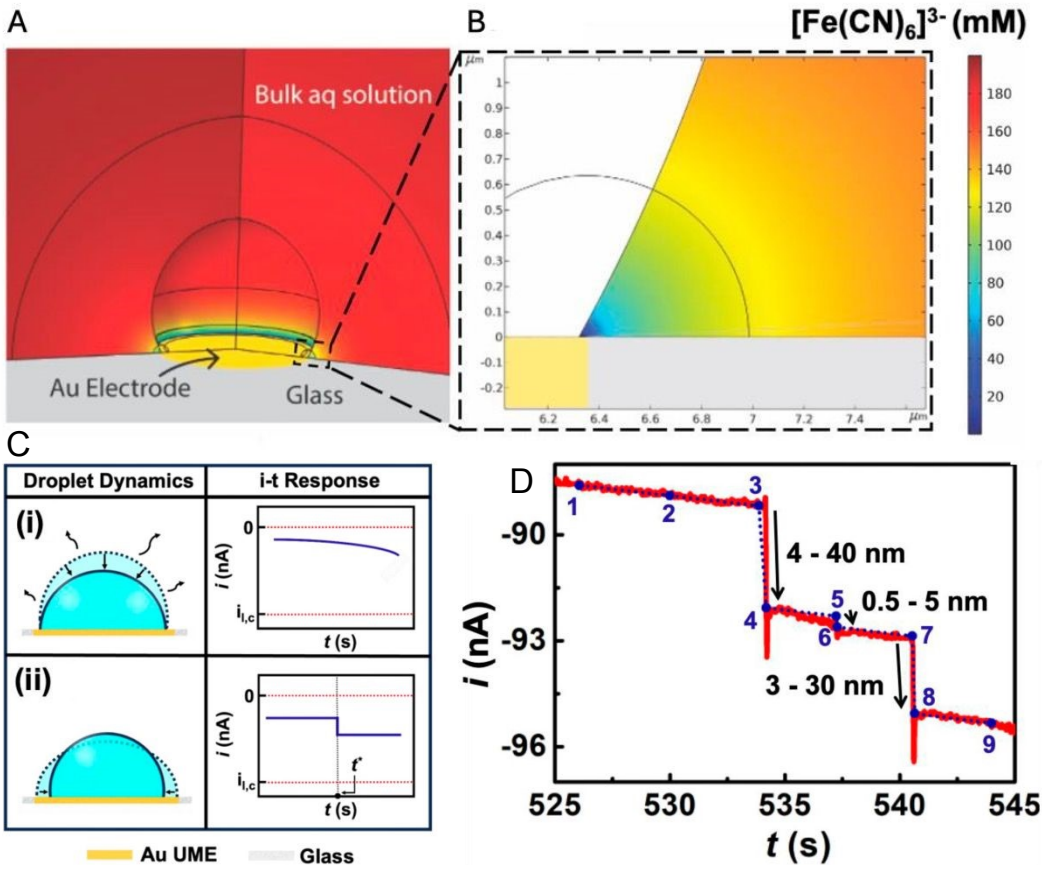

Figure 5. (A) Simulated concentration profile of $K_3[Fe(CN)_6]$ rotated around the axis of symmetry after 100 s of applying the experimental reducing potential of -0.1 V vs Ag/AgCl (the bulk solution originally contained 195 mM $K_3[Fe(CN)_6]$). (B) Inset of A showing the 2D concentration profile near the exposed portion of the electrode. (C) Two types of droplet movements used during finite element modeling: (i) a "stick" mode of dissolution where the contact area does not change but the volume decreases and (ii) a "slip" event, where the droplet suddenly decreases its contact area. The predicted amperometric (i-t) response for each droplet dynamic mode is shown in the right column. (D) Quantification of nanoscale slipping events; experimental data (solid red) can be compared to simulated (dashed blue) amperograms during the dissolution of a DCE droplet when 195 mM $K_3[Fe(CN)_6]$ is in the bulk phase. The assumed mode of dissolution between points 1-3, 4-5, 6-7, and 8-9 was constant contact radius mode, whereas slipping events were presumed to happen between points 3-4, 5-6, and 7-8. Adapted with permission from reference[70].

In our next study, we set out to verify if electrochemistry can capture nanometric movements. It is well-established that dissolving droplets function not only as sensitive microreactors for chemical analysis but also as dynamic probes of interfacial and physical properties that are difficult to access using conventional bulk techniques.

Throughout numerous trials conducted across dissolving microdroplet experiments, we observed optically that droplets would occasionally slip. These visible slipping events appeared in tandem with large current steps in electrochemical measurements[70]. It was hypothesized that slipping events can accelerate reaction rate by transiently exposing a fresh portion of the electrode surface

View Article Online
DOI: 10.1039/D6AN00461J

area. While conducting microdroplet studies, small current steps were also measured, and we hypothesized that these small current steps were the result of visually undetectable slipping events.

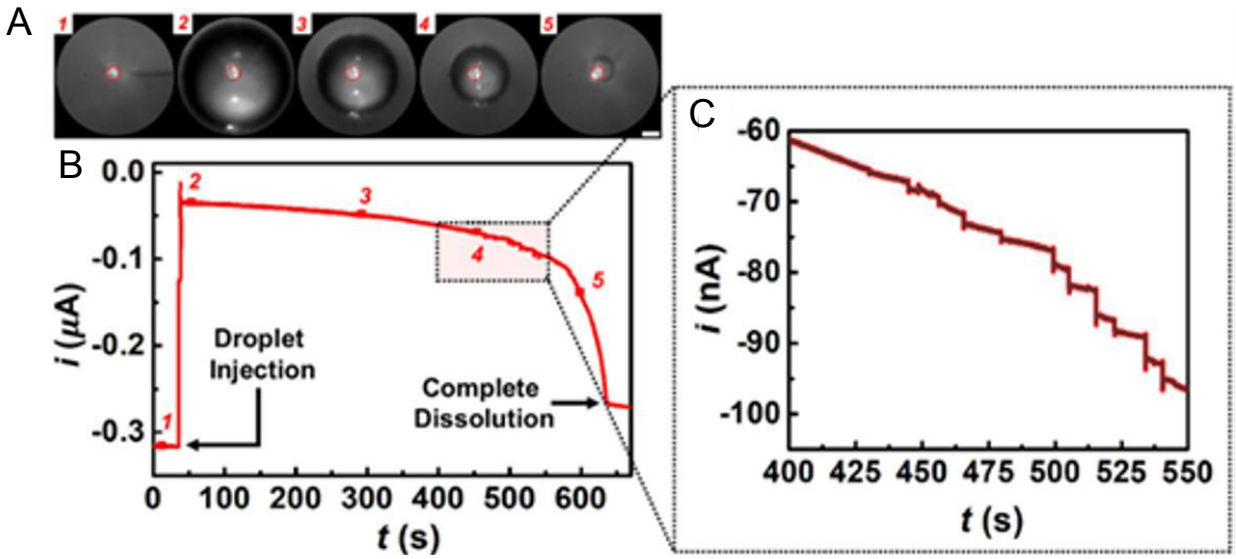

Figure 6. (A) Optical micrographs recorded during the dissolution of a 64 ± 2 µm radius DCE droplet in an aqueous bulk phase containing 195 mM $K_3[Fe(CN)_6]$. The solid red circle indicates the circumferences of the gold electrode used. Scale bar represents 20 µm. (B) Chronoamperometry of droplet dissolution featured in panel A. Numbers correspond to droplet dissolution phase illustrated in panel A. Applied potential was -0.1 V vs Ag/AgCl; chronoamperometry and images were conducted concurrently. (C) Inset of B depicting the nanoscale movements of the pinned droplet. Adapted with permission from reference[70].

For experimental validation, a finite element model was constructed to see if nanometric movements of multiphase boundaries occur, as well as whether these events were even electrochemically detectable. The time-dependent model tracks the current density on an electrode surface where a portion of the electrode surface is assumed to be blocked by an insulator (Figure 5A-B). Integrating the current density gives an initial current value, providing a baseline against which to measure a slipping event. To model the slipping event, it was imagined that the area of the electrode surface blocked by the insulator shifted some distance. This can be illustrated by simulating the concentration gradient of our redox species at the triple-phase boundary (Fig. 5B). At this point, the current can be recalculated, and the difference between this value and the baseline current provides an estimate for the change in current when a slipping event occurs. Similar to past experiments, two different modes were used in simulation: a stick mode, where the microdroplet volume changes but the contact area is static, and slip mode, where the microdroplet contact area is suddenly decreased (Fig. 5C). Figure 5C illustrates the electrochemical behavior associated with these two different modes of dissolution.

Experimentally, the DCE microdroplet was dispensed onto a gold UME and monitored both optically and electrochemically over time. The aqueous bulk solution contained $K_3[Fe(CN)_6]$ to study the flux at the electrode. Micrographs were recorded as the microdroplet dissolved, which is shown in Fig. 6A. In Fig. 6B, an i-t amperogram was recorded during the dissolution of the neat

View Article Online
DOI: 10.1039/D6AN00461J

DCE microdroplet in 195 mM $K_3[Fe(CN)_6]$. When the microdroplet is dispensed, the current is close to 0. However, as the microdroplet dissolves and the radius of the microdroplet becomes less, there is a noticeable increase in current magnitude. When the microdroplet fully dissolves, the current almost returns to the bulk current. This type of blocking experiment offers accurate measurements for the lifetime of droplets, giving us insight into dissolution dynamics of microdroplets. Furthermore, by enlarging the section of the i-t amperogram where the microdroplet is almost completely dissolved, there are small steps in current, indicating miniscule movements of the microdroplet (Fig. 6C). When measured, many of the steps were under 5 nA (Fig. 5D). These steps in current are suggestive of nanometric changes when the microdroplet suddenly slips and decreases contact area.

The COMSOL model validated that the small current steps observed in experimental i-t amperograms corresponded with simulated data (Fig. 5D). A second model was subsequently constructed to predict the electrochemical limit of detection for these slipping events. During a few hundred microsecond timescales, the model determined that appreciable current steps could arise from sub-nanometer changes in contact radius. This finding can be extrapolated to a larger time frame, and we estimate that the microdroplet radius can move tens to hundreds of nanometers in one second[70].

This section summarized the key mechanisms that dictate dissolving droplets as well as fundamental physical properties that can be extracted using finite element modeling. Within these simulations, inputting two different modes of dissolution, CCA and CCR, provided valuable insights into how these modes interact to dictate the observed electrochemical behavior of the dissolving microdroplet system. Additional simulations, coupled with experimental trials, found that droplets adsorbed to an electrode are constantly undergoing nanoscale changes in contact area, manifesting on i-t amperograms as small steps in current. Furthermore, this method can be used to electrochemically track the complete lifetime of microdroplets; which cannot be done using conventional optical microscopic techniques. Microdroplet dissolution was measured by using an oil microdroplet as an insulator and blocking detection of redox-active molecules in the aqueous phase until the microdroplet dissolved to a sufficiently small contact area. The microdroplet lifespan is monitored as the gradual appearance of redox activity on electrochemical readings, followed by a steady-state current, indicates complete dissolution. Importantly, gaining information about complete microdroplet dissolution enables a straightforward calculation of the liquid-into-liquid diffusion coefficient for different organic phases into the aqueous phase. In the next section, we discuss using the electroanalytical strategy of dissolving microdroplets to access ultralow detection of the analyte of interest. Methods such as concentration enrichment and signal amplification were employed to allow down to attomolar detection.

Dissolving Droplets as an Electroanalytical Sensor

Dissolving Droplets Enable Nanomolar Detection

View Article Online
DOI: 10.1039/D6AN00461J

Solution evaporation has been used as a concentration enrichment technique since the 1600s[87], however, it wasn't until 1997 that a paper was published in Nature describing the concentration enrichment effects that occur when a microdroplet dissolves[88]. As the volume of the solvent decreases, the concentration of the analyte increases. The analytical techniques that are traditionally paired with evaporative enrichment generally require quantification in relatively large volumes. Evaporation techniques, such as microarray and levitating droplets, commonly use larger volume droplets (diameter ≥ 1.0 mm) [37,89]. This often limits their ability to directly interrogate the evolving chemistry of individual microdroplets. Electrochemistry is a powerful tool for probing extremely small volumes, offering robust and quantitative measurements at the femtoliter to attoliter levels. This capability allows for the ability to track microdroplet behavior and detection at very low concentrations. In this section, we will discuss the electroanalytical strategies for trace concentration quantification in dissolving droplets.

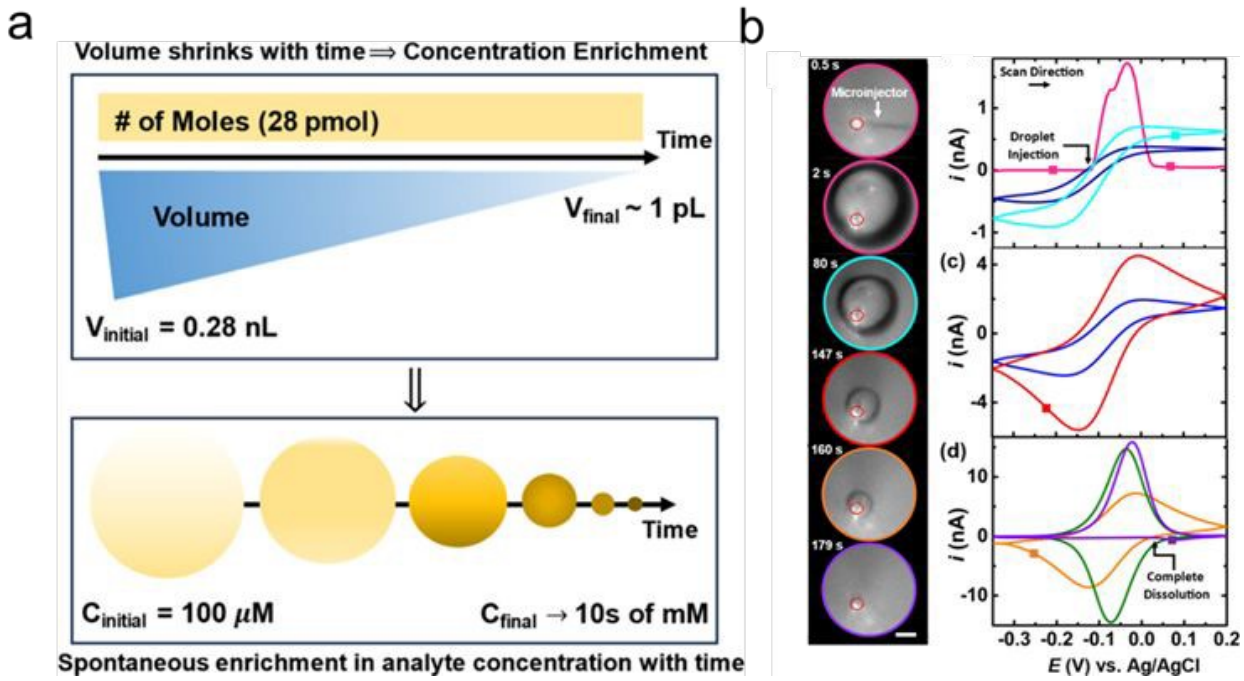

Figure 7. (A) Schematic illustrating the process of concentration enrichment in a dissolving microdroplet (B) Optical micrographs recorded for the dissolution of a microdroplet containing 100 μM $(Cp^*)_2Fe^{II}$ in a 10 mM $NaClO_4$ aqueous bulk phase. The scale bar is 25 μm. Figure adapted with permission from reference[67].

For this series of experiments, the electrochemical set-up consisted of a vertically oriented gold disk ultramicroelectrode, inserted in a Teflon cell containing the aqueous electrolyte $NaClO_4$[66]. We dissolved decamethyl ferrocene ($(Cp^*)_2Fe^{II}$) in the DCE phase and dispensed the microdroplet onto a gold micro-disk using a glass micropipette. This redox species was selected due to its low solubility in water, which promotes strong partitioning into the DCE microdroplet. $(Cp^*)_2Fe^{II}$ undergoes a reversible one-electron oxidation to $(Cp^*)_2Fe^{III}$, and charge balance is maintained by ClO_4^- anions partitioning from the aqueous phase into the organic phase. A three-axis micropositioner and pneumatic compressor were used to precisely disperse the microdroplet atop the electrode. A camera mounted above the cell allowed visualization of the system to accurately

View Article Online
DOI: 10.1039/D6AN00461J

align the micropipette with the gold micro-disk and track microdroplet radius changes over time. Bright-field optical images of the electrode surface are collected in reflectance mode under diffuse white-light illumination. Electrochemical measurements were carried out using a two-electrode configuration, with the reference/counter electrode placed in a separate reservoir containing 1 M KCl. The separate reservoir was connected to the main cell via an agarose salt bridge.

In this section, we study concentration enrichment arising from microdroplet dissolution and outline the underlying mechanism using a schematic representation of the process which can be shown in Fig 7A[67]. The enrichment of the redox-active species is governed by the total quantity of analyte initially confined within the microdroplet, which is determined by both the starting microdroplet volume deposited on the Au micro-disk and the initial analyte concentration. As the microdroplet dissolves, the total number of redox-active molecules remains constant, provided that the analyte does not partition across the oil|water interface[67]. The most effective method to guarantee that no partitioning occurs is to purposefully select an analyte that is highly insoluble in aqueous environments.

When the microdroplet nears complete dissolution, the microdroplet volume is within the picoliter regime, leading to effective analyte concentrations on the order of tens of millimolar and an enrichment factor exceeding two orders of magnitude. This enrichment strategy markedly improves the sensitivity of voltammetric measurements, enabling detection of analyte concentrations in the nanomolar range levels, which is traditionally inaccessible using conventional bulk electrochemical approaches[67].

These physical concentration shifts throughout dissolution are reflected electrochemically in voltammetric curves (Fig. 7B-D). After the injection of the microdroplet, there is a positive surge of current because injection induces a massive flux of $(Cp^*)_2Fe^{II}$ at the electrode surface. We initially observe a sigmoid-shaped voltammogram at the max microdroplet size (cyan curve on Fig. 7B). This signal is expected since the large microdroplet size mimics bulk-like conditions on a UME. When the microdroplet is large (bulk-like condition), the electrode cannot probe the entirety of the volume, and redox activity is confined near the electrode surface. As the microdroplet gets smaller in volume, we notice the appearance of peaks on the voltammograms (red curve on Fig 7C). This "peaking" behavior gets more intense with time, eventually leading to a Gaussian-shaped pair of peaks reaching a current of ~ ±10 nA (green curve on Fig 7D). These peaks imply that the microdroplet has reached thin-layer conditions, meaning that the size of the microdroplet is comparable to the size of the electrode and voltammetry can probe all redox active molecules present in one cycle[66].

This study increased our understanding of concentration enrichment behavior in voltammetric curves, and we leveraged this characterization to detect nanomolar concentrations of $(Cp^*)_2Fe^{II}$ in DCE[67]. The potential of the UME was cycled between an initial potential of −0.35 V and 0.2 V vs Ag/AgCl at a scan rate of 0.2 V/s. The potential windows were chosen so that the apparent standard potential of the redox couple $(Cp^*)_2Fe^{II}/(Cp^*)_2Fe^{III}$ ($E°'$= −0.10 V) was centered around the

View Article Online
DOI: 10.1039/D6AN00461J

potential window of voltammetry. Optical micrographs were recorded in tandem with voltammetry (Fig. 8). The experiment started when the microdroplet was dispensed at t = 0.5 s with an initial microdroplet size of 64 µm. The microdroplet was pinned to the Au micro-disk and stayed on the electrode for the entire duration of the dissolution. Voltammetry was recorded and can be seen and Fig. 8B, C. There was no notable redox activity when the microdroplet was large, which can be shown in Fig. 8B. As the microdroplet dissolved, there was a surge of current that can be seen in Fig. 8C. When the microdroplet reached the same size as the electrode, allowing electrochemical access to the entire volume, the largest magnitude of current can be observed as a result (purple voltammogram in Fig. 8C). The microdroplet size is shown in Fig. 8A. Furthermore, from the highest magnitude redox peak, charge quantification can be characterized. Figure 8D shows the evolution of the radius of the microdroplet as a function of time and illustrates the occurrence of redox activity with the decreasing size of the microdroplet.

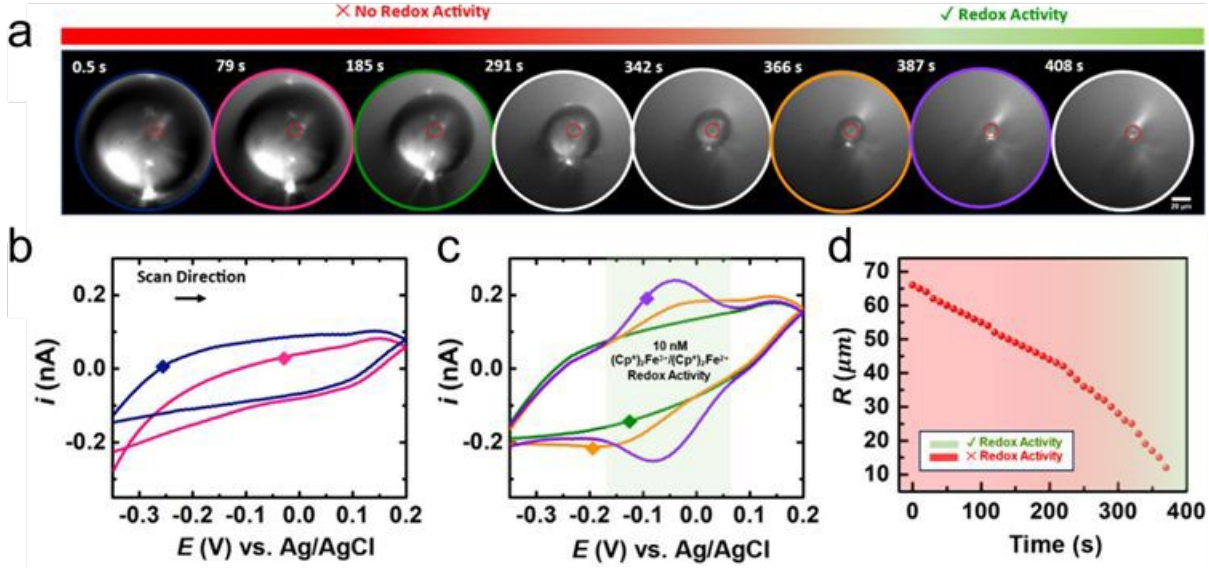

Figure 8. (A) Optical micrographs recorded during dissolution of a dissolving microdroplet containing 10 nM $(Cp^*)_2Fe^{II}$ in a 10 mM $NaClO_4$ aqueous bulk phase. (B) Cyclic voltammograms recorded whiles the microdroplet is large, which shows no redox activity. (C) Cyclic voltammograms recorded while the microdroplet is small, which shows little to maximum redox activity. (D) Apparent microdroplet's radius as a function of time measured from the optical micrographs in panel (A), showing the appearance of redox activity of $(Cp^*)_2Fe^{II}$/ $(Cp^*)_2Fe^{III}$. Figure adapted with permission from reference[67].

The charge quantification from the redox peak can determine the unknown concentration of the redox analyte (Eq. 2).

$$Q = nFCV \qquad \text{(Equation 2)}$$

where Q is the charge (Coulombs), n is the number of electrons transferred, F is Faraday's constant (96,485 C/mol), and V is the volume of the microdroplet (m^3).

Before detecting nanomolar concentrations, we first confirmed that sub-µM detection was possible using this methodology. To ensure ethical and rigorous testing, we performed a blind study: one

View Article Online
DOI: 10.1039/D6AN00461J

lab member prepared a known solution of 800 nM $(Cp^*)_2Fe^{II}$ in DCE and another quantified the concentration using the dissolving microdroplet method[67]. Correlated optical micrographs tracking microdroplet size and cyclic voltammograms from this experiment are illustrated in Fig. 9. The maximum redox peak in the CV was used to calculate the charge, and Faraday's law was used to deduce the initial concentration of the redox analyte based on the value of charge and the initial volume of the microdroplet (Eq. 2). The initial volume was calculated to be 0.45 nL and charge associated with the highest redox peak was measured to be 24 pC. Using these values, the concentration of the analyte in the unknown test sample was found to be 500 nM[67]. The relative error was found to be approximately 35%. This error likely originates from the partitioning of $(Cp^*)_2Fe^{II/III}$ species across the oil|water interface into the aqueous bulk phase. Given the low concentration, the measurement precision is quite robust, even with this effect.

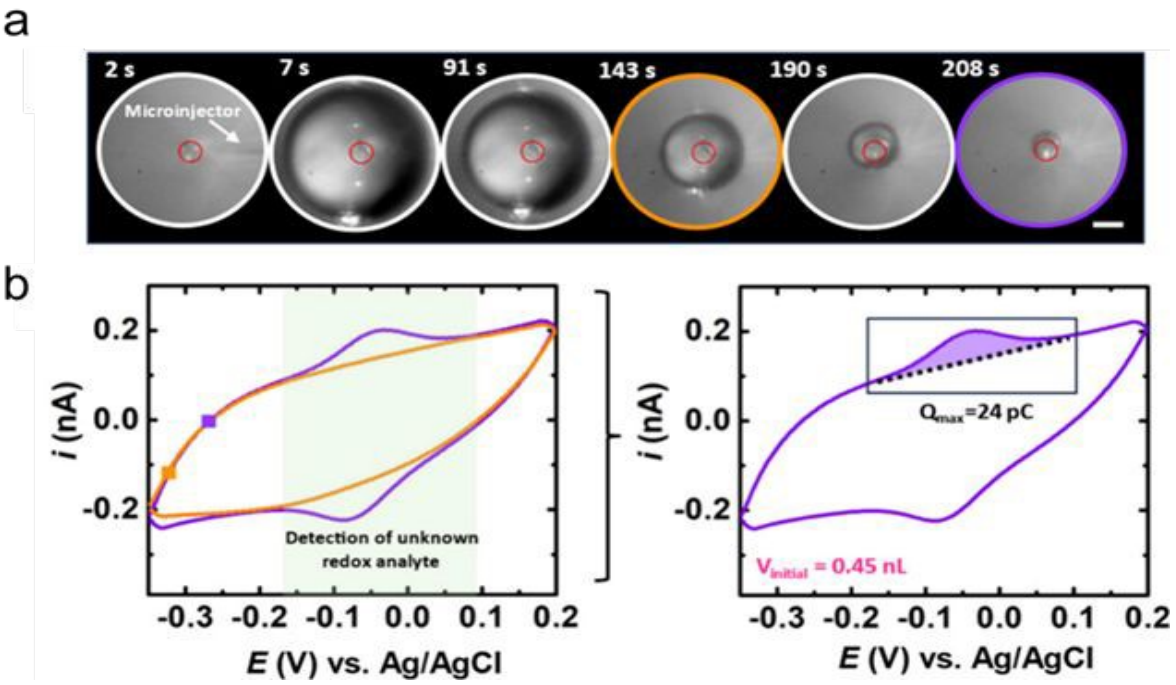

Figure 9. (A) Optical micrographs recorded during the dissolution of a DCE microdroplet containing 800 nM $(Cp^*)_2Fe^{II}$. (B) Cyclic voltammograms recorded during the dissolution of the DCE microdroplet along with the charge calculation for the voltammogram with redox activity. The scale bar is 20 μm. Figure adapted with permission from reference[67].

With just concentration enrichment alone, $(Cp^*)_2Fe^{II}$ could be detected at sub-nanomolar levels. In the next work, we further decrease the LOD by amplifying the signal with an EC' reaction. An EC' reaction is an electron-transfer reaction (E) coupled with a chemical reaction (C) where the species involved in the electron transfer reaction is regenerated. In addition to those analytes, different concentrations of potassium ferricyanide ($K_3[Fe(CN)_6]$) were spiked into the aqueous solution to trigger the EC′ mechanism (Fig. 10Ai).

In a typical experiment, a DCE microdroplet spiked with $(Cp^*)_2Fe^{II}$ is injected and positioned onto an Au UME using a microinjector (Fig. 10A). The aqueous phase contained varying concentrations of $K_3[Fe(CN)_6]$ across experiments, along with 10 mM $NaClO_4$. As the microdroplet dissolves,

View Article Online
DOI: 10.1039/D6AN00461J

electrochemical measurements are conducted concurrently with real-time monitoring of the microdroplet's geometry using a high-resolution camera. Micrographs are acquired in brightfield mode using diffuse white light illumination. All electrochemical measurements were conducted using a two-electrode setup. The working electrode was an Au UME and the reference/counter electrode was Ag/AgCl in 1 M KCl. An agarose salt bridge was used to connect the reference/counter electrode to the main cell. Within the biphasic system, the microdroplet initially contains only $(Cp^*)_2Fe^{II}$ molecules but will spontaneously react with $Fe(CN)_6^{3-}$ (shown as Fe^{III}) and oxidize to $(Cp^*)_2Fe^{III}$ at the oil–water interface[68]. Inset (i) in Fig. 10A shows the spontaneous chemical reaction at the liquid-liquid boundary with $(Cp^*)_2Fe^{II}$ and $K_3[Fe(CN)_6]$. This biphasic reaction requires the partitioning of ClO_4^- ions from the aqueous phase to the oil phase to maintain electroneutrality, although no potential is necessary for this reaction.

View Article Online
DOI: 10.1039/D6AN00461J

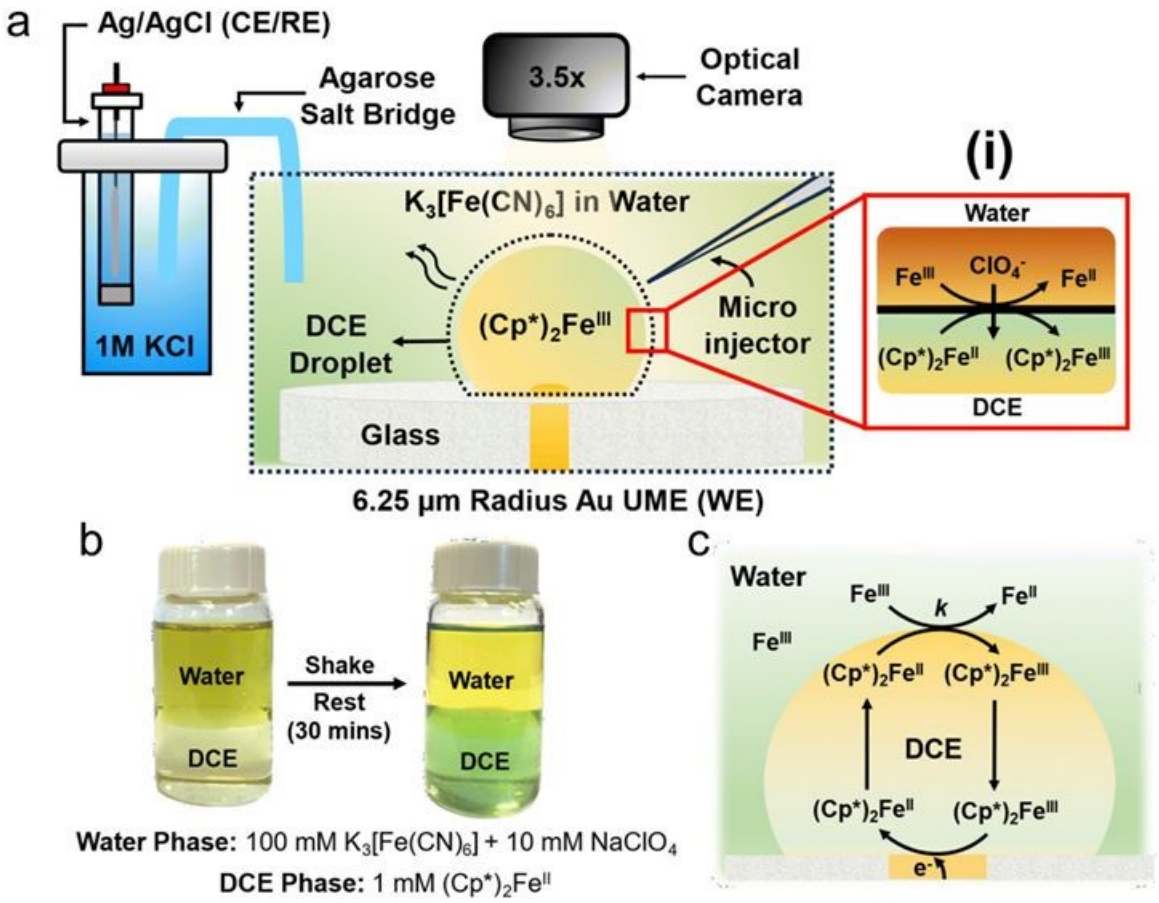

Figure 10. (A) Experimental setup illustrating the components: $(Cp^*)_2Fe^{II}$ in a DCE droplet, $K_3[Fe(CN)_6]$ in the aqueous bulk phase. The cell comprises an Au UME, Microinjector, and an agarose salt bridge connecting to a 1 M KCl reservoir with the CE/RE Ag/AgCl. Experiment monitoring is facilitated by an optical camera. (i) Chemical reaction at the oil|water interface, where $Fe(CN)_6^{3-}$ denoted as Fe^{III} is reduced to $Fe(CN)_6^{3-}$, denoted as Fe^{II}, and $(Cp^*)_2Fe^{II}$ oxidizes to $(Cp^*)_2Fe^{III}$, with ClO_4^- transitioning between the phases to maintain electroneutrality. (B) Shake-flask experiment where the water phase contains 100 mM $K_3[Fe(CN)_6]$ and 10 mM $NaClO_4$, while the DCE phase contains 1 mM $(Cp^*)_2Fe^{II}$. After shaking and resting for 30 minutes, the DCE phase changes to a green color, indicating oxidation of $(Cp^*)_2Fe^{II}$. (C) Mechanism of the EC′ reaction in a droplet. This figure was used with permission from reference[68].

To validate that the biphasic reaction is occurring, a shake flask test with equal parts water and oil was performed to see the chemical reaction across the liquid-liquid boundary[90]. The DCE had $(Cp^*)_2Fe^{II}$ (light-yellow color) and the water phase had $K_3[Fe(CN)_6]$ and $NaClO_4$ (dark-yellow color). The vial was shaken until an emulsion formed and it was left to rest for 30 minutes. After 30 minutes, the oil phase is fully green as all the $(Cp^*)_2Fe^{II}$ has oxidized to $(Cp^*)_2Fe^{III}$. In the water phase, the yellow saturation slightly increases as $Fe(CN)_6^{3-}$ is reduced to $Fe(CN)_6^{4-}$. Although the shake flask experiment illustrates the spontaneous reaction, there is no regeneration of the $(Cp^*)_2Fe^{II}$. For the dissolving microdroplet system, the electrochemical reaction regenerates $(Cp^*)_2Fe^{II}$ from $(Cp^*)_2Fe^{III}$ and the spontaneous reaction can be repeated; this results in a

View Article Online
DOI: 10.1039/D6AN00461J

significant signal amplification and can be characterized as an EC' reaction. The mechanism for this experiment is in Fig. 10C.

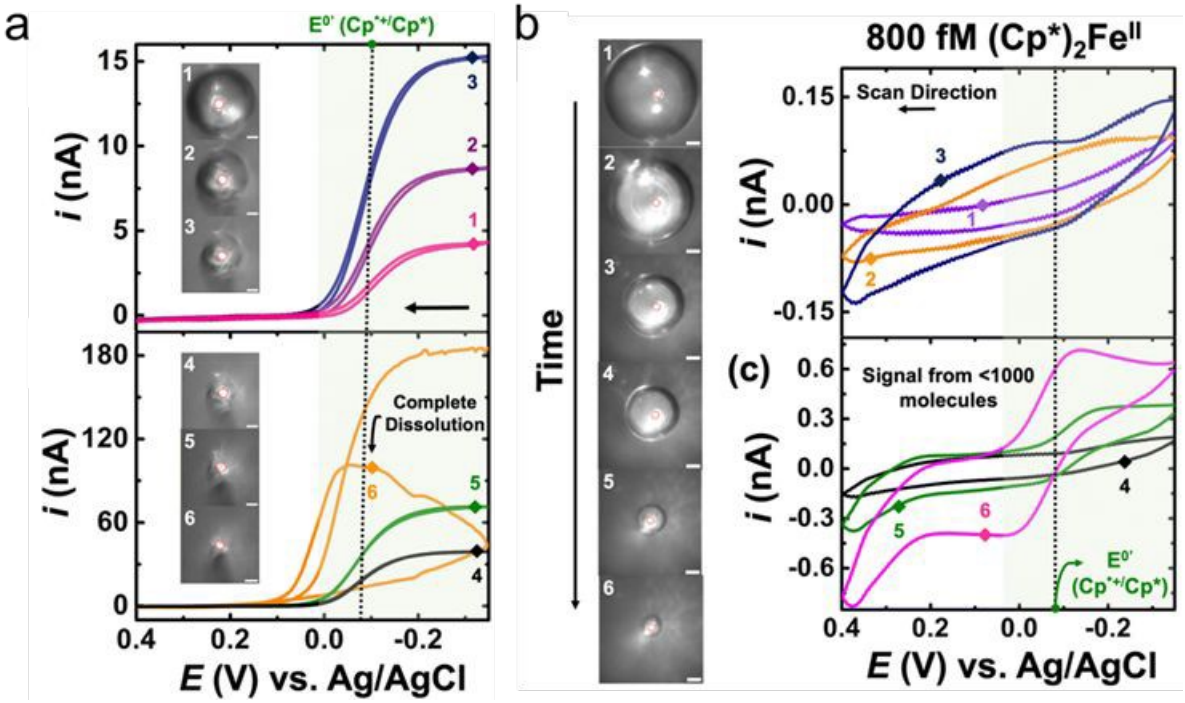

Figure 11. (A) Cyclic voltammograms recorded during this dissolution of DCE droplet containing 0.5 mM $(Cp^*)_2Fe^{II}$. The aqueous bulk phase contains 100 mM $K_3[Fe(CN)_6]$ and 10 mM $NaClO_4$ in water. The dotted line marks the apparent standard potential for the redox couple $(Cp^*)_2Fe^{III}/(Cp^*)_2Fe^{II}$. The numbered points on the cyclic voltammogram indicate the exact time at which the numbered micrographs were recorded. (B) Optical micrographs recorded during the dissolution of DCE droplet containing 800 fM of $(Cp^*)_2Fe^{II}$ in an aqueous bulk phase containing 50 μM $K_3[Fe(CN)_6]$ and 10 mM $NaClO_4$. Cyclic voltammograms were recorded during the dissolution of the DCE. The voltammetric curves are numbered to correspond with the micrographs, indicating the size of the droplet during the voltammetric sweep. The scale bar for the micrographs is 20 μm. Figure taken with permission from reference[68].

One of the starting goals was to witness the voltametric response of an EC' experiment. The DCE microdroplet was spiked with 0.5 mM $(Cp^*)_2Fe^{II}$ and the aqueous phase contained 100 mM $K_3[Fe(CN)_6]$ and 10 mM $NaClO_4$. The spiking of $K_3[Fe(CN)_6]$ started with adding 1.4 mL of 10 mM $NaClO_4$ into the electrochemical cell. A DCE microdroplet with 0.5 mM $(Cp^*)_2Fe^{II}$ was then injected and positioned onto the Au disk. After injection, 1.4 mL of a solution of 200 mM of $K_3[Fe(CN)_6]$ and 10 mM of $NaClO_4$ was added into the same cell equaling the desired concentration $K_3[Fe(CN)_6]$ in the bulk phase. It is essential to use such a strategy to avoid interference in the redox activity of Cp* from of $K_3[Fe(CN)_6]$. The experimental results along with their corresponding optical images are shown in Fig. 11A. Cyclic voltammograms were recorded in a potential window of −0.35 V to 0.4 V vs Ag/AgCl at a scan rate of 0.2 V s^{-1}. The redox activity is observed at the apparent standard potential for the redox couple $(Cp^*)_2Fe^{III}/(Cp^*)_2Fe^{II}$ (−0.1 V vs Ag/AgCl). This potential is represented by a dotted line and a green shade showing $(Cp^*)_2Fe^{III}/(Cp^*)_2Fe^{II}$ redox activity. In a normal dissolving microdroplet setup, the

View Article Online
DOI: 10.1039/D6AN00461J

voltammograms would evolve from sigmoidal to duck-shaped and ultimately Gaussian peaks, however, with this setup, only sigmoid shaped voltammograms are present. The reason for this is that at any given moment within the microdroplet, the redox analyte exists in its oxidized form, $(Cp^*)_2Fe^{III}$ due to the reaction occurring at the oil|water interface. As the microdroplet dissolves, the current will rise, most notably after the addition of $K_3[Fe(CN)_6]$ into solution.

Dissolving Droplets Coupled with EC' Mechanism Enable Sub-Picomolar Detection

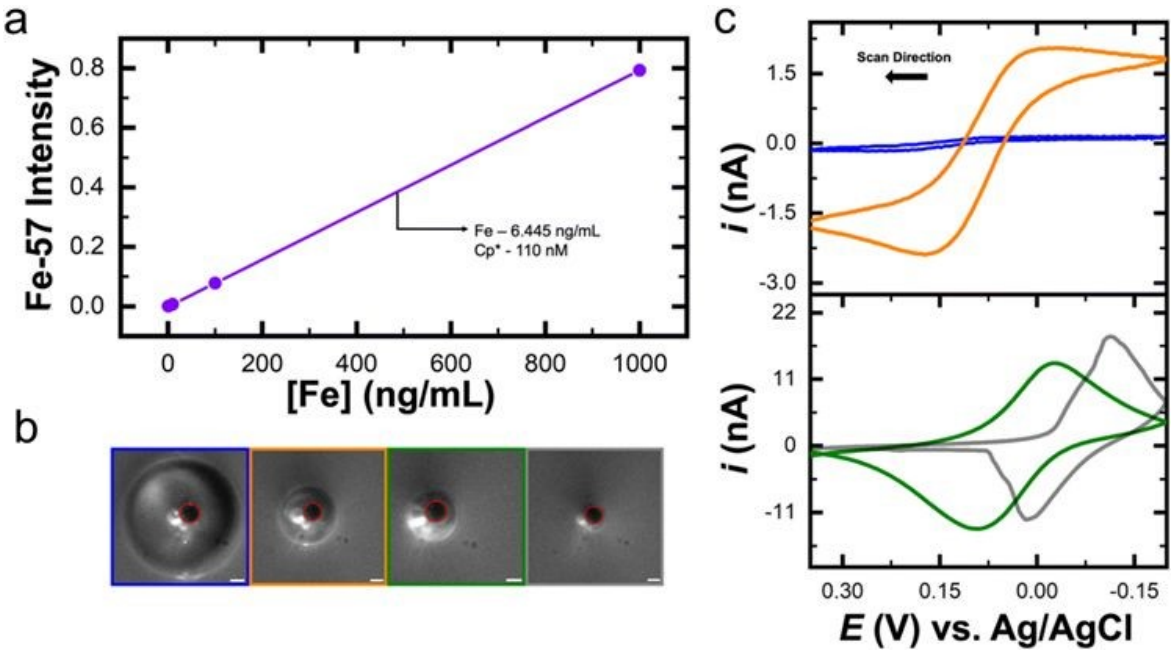

Figure 12. (A) ICP-MS calibration curve for the determination of trace Fe in unknown solution. (B) Optical micrographs recorded for the dissolution of a neat DCE microdroplet as $(Cp^*)_2Fe^{II}$ continuously partition into the microdroplet from the bulk phase. The scale bar for the micrographs is 10 µm (C) Cyclic voltammograms were recorded at different time points over an 11-minute dissolution period to show electrochemical response at starting radius of 51 µm microdroplet size to near complete dissolution of the microdroplet at 7 µm radius microdroplet size. Figure taken from reference[90] with permission.

Coupling dissolving droplets with the EC' mechanism enables unprecedented electrochemical access to sub-pM detection levels of $(Cp^*)_2Fe^{II}$ [90]. The concentration of our analyte (800 fM $(Cp^*)_2Fe^{II}$) and concentration of $K_3[Fe(CN)_6]$ (50 µM) were adjusted for ultralow concentration detection. The scan rate was increased to 1 V/s to measure the electrochemical response. The voltammograms show that as the microdroplet dissolves, there is an electrochemical response for $(Cp^*)_2Fe^{II}$ with a maximum redox peak which can be shown as the pink curve in Fig. 11B. The number of molecules calculated was found to be approximately 1000 molecules. This study introduces an electrochemical platform capable of detecting fewer than 1000 molecules of redox analyte by signal amplification through EC' catalysis with dissolving microdroplet[90].

Previously, the LOD was lowered through EC' catalysis. In this study, we lower the LOD further by leveraging partitioning kinetics of our analyte, allowing us to detect attomolar concentrations of redox-active analytes. While the redox-active analyte $(Cp^*)_2Fe^{II}$ is relatively insoluble in water,

View Article Online
DOI: 10.1039/D6AN00461J

trace amounts will still dissolve. We confirmed the solubility limit of $(Cp^*)_2Fe^{II}$ in water with ICP-MS (Fig. 12A). It was found that a concentration of 110 nM could be dissolved in water. This concentration of $(Cp^*)_2Fe^{II}$ was dissolved into the aqueous bulk and it was observed that the analyte partitioned into the DCE microdroplet where the signal could easily be quantified (Fig. 12B-C). Initially, the CVs are sigmoid-shaped, but as the microdroplet dissolves, the signal evolves into a duck-shape voltammogram. When the microdroplet shrunk to the size of the electrode, Gaussian peaks appeared (gray curve), signifying thin-layer conditions.

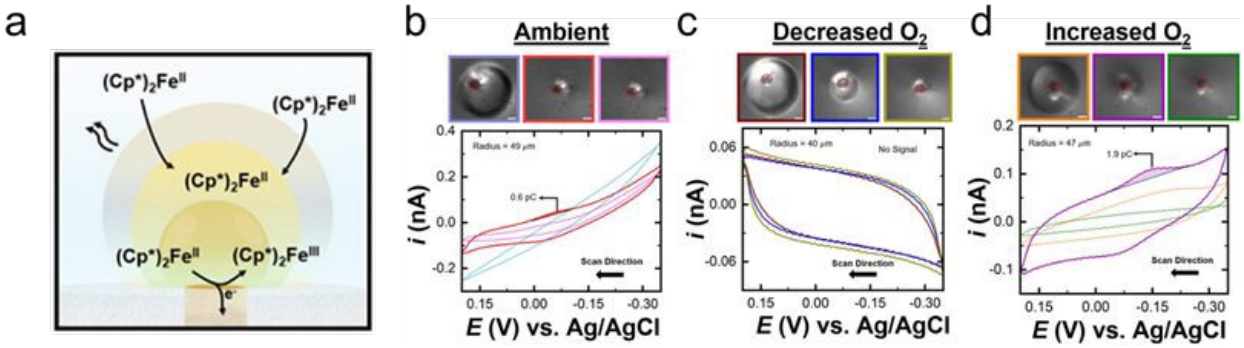

Figure 13. (A) A schematic of a proposed mechanism of $(Cp^*)_2Fe^{II}$ partitioning into the DCE microdroplet. (B) Cyclic voltammograms recorded at ambient conditions with optical micrographs depicting decreasing microdroplet size. (C) Cyclic voltammograms recorded in argon rich conditions with optical micrographs depicting decreasing microdroplet size. (D) Cyclic voltammograms recorded at oxygen rich conditions. The aqueous bulk phase contains 1 aM $(Cp^*)_2Fe^{II}$ and 10 mM $NaClO_4$ in water. The scale bar for the micrographs is 10 μm. Figure adapted with permission from reference[90].

After confirming that we could detect 110 nM of $(Cp^*)_2Fe^{II}$, we further diluted this concentration down to 1 aM and were still able to successfully detect this concentration[90]. To clarify, we dissolved 1 aM of $(Cp^*)_2Fe^{II}$, together with 10 mM $NaClO_4$, into the aqueous bulk phase surrounding the DCE droplet. Assuming a bulk solution volume of approximately 2 mL, this corresponds to slightly more than one thousand analyte molecules distributed throughout the solution. Because $(Cp^*)_2Fe^{II}$ preferentially partitions into the DCE phase, the analyte rapidly diffuses into the DCE droplet and produces substantial local concentration enrichment relative to the initial bulk concentration. Consequently, although the bulk aqueous concentration of $(Cp^*)_2Fe^{II}$ remains 1 aM, the effective concentration within the DCE droplet reaches the picomolar-to-femtomolar range due to the extremely small solvent volume. As the microdroplet continues to dissolve and decrease in volume, the local analyte concentration increases further. This measurement illustrates the effectiveness of leveraging analyte partitioning characteristics and concentration enrichment from a dissolving microdroplet. The mechanism for attomolar detection is shown in Fig. 13A. The potential was swept from −0.2 V to 0.35 V vs Ag/AgCl at a scan rate of 1 V s^{-1}. At ambient conditions, the redox peak for $(Cp^*)_2Fe^{II}$ could be determined. The voltammograms at ambient conditions along with their optical micrographs can be seen in Fig. 13B.

View Article Online
DOI: 10.1039/D6AN00461J

Interestingly, while the charge can be measured from voltammograms at 0.6 pC, the expected (calculated) charge was much smaller at 0.29 fC. This discrepancy is likely because O_2 is playing a role, as it is the most likely candidate to participate in redox reaction compared to the other species in the solution. The dissolved O_2 is most likely amplifying the signal through an EC' reaction with $(Cp^*)_2Fe^{II}$ and O_2. Further confirmation of O_2's role in signal amplification can be studied through control experiments with inert gas, ambient, and O_2 saturated conditions with different analyte concentrations. If it was not O_2, but reactive redox intermediates, spectroscopic tools can be employed to rule out any redox intermediates that could affect the signal. Although the exact role of O_2 in the observed electrochemical behavior has not yet been fully elucidated, our group is actively investigating the associated reaction mechanisms, along with the influence of confinement in a biphasic environment and interfacial boundary effects on oxygen reactivity. The voltammograms for detection of 1 aM in the presence of argon and without argon are shown in Fig. 13B-D. Removing O_2 from the system resulted in no detectable redox peaks, whereas increasing O_2 optimized observed redox peaks. Saturating the system with O_2 increased the measured charge threefold, with a measured charge of 1.9 pC. The voltammogram and optical micrographs for increased O_2 are in Fig. 13D. These results demonstrated that O_2 saturation significantly amplified the electrochemical response from $(Cp^*)_2Fe^{II}$. The presence of dissolved oxygen significantly impacted the kinetics of the EC' reaction. At lower concentrations of $(Cp^*)_2Fe^{II}$, O_2 facilitates signal amplification through EC', suggesting the true LOD is much lower than attomolar levels[90].

This section summarizes the development of a new concentration enrichment electroanalytical technique that couples dissolving droplets, EC' reaction schemes, and partitioning kinetics to achieve sub-ppq ($<10^{-15}$), or attomolar, quantification. This technique uses three concentration enrichment methods: first, an analyte is selected that will partition from the aqueous phase into the organic microdroplet, magnifying the concentration exponentially, specifically in ambient or O_2 saturated conditions, as the volume of solvent is drastically reduced. A second criterion is to select an organic microdroplet that is partially soluble in water, so that over time it will dissolve into the aqueous continuous phase. As the microdroplet dissolves into the bulk, the concentration of the analyte scales cubically with the volume decrease. Finally, by using an EC' reaction scheme, the analyte can be replenished, enriching the concentration of the original species. Combined, these concentration enrichment effects allow quantification of attomolar concentrations.

Future Directions/Conclusion

There remains substantial opportunity to expand this electroanalytical dissolving microdroplet technique beyond its current scope. To date, it has primarily been used to isolate unique microdroplet characteristics, such as diffusion coefficients, microdroplet lifetime, and nanoscale movements. The dissolution coefficients and microdroplet lifetimes of both DCE and nitrobenzene microdroplets were identified; however, this methodology can be expanded to include any organic solvent that is slightly miscible in water over time. Further experimentation can be done to confirm

View Article Online
DOI: 10.1039/D6AN00461J

this principle, and relevant statistics can compare these values to literature. The inverse can also be monitored by dispersing a water microdroplet in various organic solvents.

This platform can also be used as a sensing method and can measure attomolar concentrations, depending on the analyte of choice. A natural extension is its application to trace metal detection, such as lead, arsenic, and cadmium in environmental samples, where ultralow limits of detection are critically important. An additional application that could be explored is quantifying electroactive biological molecules in complex matrices, such as blood or urine, enabling medically relevant trace analysis. Furthermore, while it is evident that oxygen plays a role in amplifying the signal to measurable peaks, additional experimentation is necessary to confirm the mechanism by which it does so. Although the mechanism is unknown, oxygen saturation can be incorporated into future application studies for signal amplification.

While this technique has not yet been evaluated in complex chemical matrices, differences in species solubility may be leveraged to achieve selective measurements. In particular, an organic droplet dispersed within an aqueous bulk phase (and vice versa) could enable preferential partitioning of target organic analytes into the droplet, allowing both concentration enrichment and diffusion-driven extraction from a matrix containing other chemical species[90]. This approach may therefore permit measurement of analytes at low concentrations while reducing interference from non-partitioning species. Additionally, the choice of organic phase provides another level of control, as the diffusion behavior of the analyte can be tuned through solvent selection to further enhance selectivity. However, future studies are needed to systematically evaluate matrix effects and the overall selectivity of the method.

However, several practical limitations must be considered. The method inherently requires an electroactive analyte; non-electroactive species cannot be detected without derivatization. Similarly, analytes that are even moderately miscible in both aqueous and organic phases may not partition sufficiently to achieve meaningful enrichment. Selectivity also remains largely untested. Matrix effects could prove detrimental, particularly in samples containing multiple electroactive species. If redox-active compounds exhibit similar half-wave potentials, peak overlap may complicate deconvolution and quantitative analysis. Addressing these selectivity and matrix challenges will be essential before the technique can be broadly applied to real-world environmental or biological systems.

This review demonstrates that coupling electrochemical measurements with dissolving droplets provides valuable insights into microdroplet dynamics. Subtle nanoscale movements of surface-pinned microdroplets manifest as discrete steps in chronoamperometric traces, allowing high-resolution tracking of microdroplet motion. By introducing a redox-active analyte in the bulk and positioning an insulating organic microdroplet atop the electrode, nanoscale displacements can be quantified electrochemically. Our results demonstrate that dissolving microdroplets pinned to the surface are not static but exhibit nanometric dynamics that are not readily observable by optical

View Article Online
DOI: 10.1039/D6AN00461J

microscopy. In this context, electrochemistry provides resolution beyond that of conventional imaging techniques. This platform also enables extraction of fundamental physical parameters, including the diffusion coefficient of dichloroethane into water and the lifetime of individual microdroplets.

Finally, dissolving microdroplets can function as a concentration enrichment strategy, significantly enhancing electrochemical performance and analytical capability. Specifically, the limit of detection for a 6.3 μm radius gold ultramicroelectrode was reduced from nanomolar (10^{-9} M) concentrations in bulk solution to attomolar (10^{-18} M) concentrations within a dissolving organic microdroplet[67,68,90]. Beyond sensitivity improvements, this approach enables analyte isolation through phase partitioning: species that are only partially soluble in the bulk phase can accumulate in the microdroplet, facilitating separation and quantification at ultratrace levels. These findings highlight the technique's dual analytical and mechanistic utility, while underscoring the need for future studies focused on selectivity, matrix tolerance, and practical implementation in environmental and biological detection.

Author Contribution

S.M.H and J.H.N contributed equally to this work. All authors have agreed to the final version of the manuscript.

Conflicts of Interest

J.E.D. and A.R. are coinventors on U.S. Patent US 12,517,083 B2 related to microdroplet-based electroanalytical techniques discussed in this method.

Bottom of Form

Acknowledgments

This work was funded by the National Science Foundation under grant CHE-2403964. The authors acknowledge the use of Chat GPT-5.4 for language refinement.

References

(1) Scholz, F. The Electrochemistry of Particles, Droplets, and Vesicles-the Present Situation and Future Tasks. *Journal of Solid State Electrochemistry*. July 2011, pp 1699–1702. https://doi.org/10.1007/s10008-011-1318-7.

(2) Kwon, S. J.; Zhou, H.; Fan, F. R. F.; Vorobyev, V.; Zhang, B.; Bard, A. J. Stochastic Electrochemistry with Electrocatalytic Nanoparticles at Inert Ultramicroelectrodes -

View Article Online
DOI: 10.1039/D6AN00461J

Theory and Experiments. *Physical Chemistry Chemical Physics* **2011**, *13* (12), 5394–5402. https://doi.org/10.1039/c0cp02543g.

(3) Singh, P. S.; Lemay, S. G. Stochastic Processes in Electrochemistry. *Analytical Chemistry*. American Chemical Society May 17, 2016, pp 5017–5027. https://doi.org/10.1021/acs.analchem.6b00683.

(4) Moazzenzade, T.; Huskens, J.; Lemay, S. G. Stochastic Electrochemistry at Ultralow Concentrations: The Case for Digital Sensors. *Analyst*. Royal Society of Chemistry February 7, 2020, pp 750–758. https://doi.org/10.1039/c9an01832h.

(5) Vannoy, K. J.; Lee, I.; Sode, K.; Dick, J. E. Electrochemical Quantification of Accelerated FADGDH Rates in Aqueous Nanodroplets. *Proceedings of the National Academy of Sciences* **2021**, *118* (25). https://doi.org/10.1073/pnas.2025726118.

(6) Bard, A. J.; Faulkner, L. R. *Electrochemical Methods: Fundamentals and Applications*; John Wiley & Sons, Inc., 2001.

(7) Wang, Y.; Shan, X.; Tao, N. Emerging Tools for Studying Single Entity Electrochemistry. *Faraday Discuss.* **2016**, *193*, 9–39. https://doi.org/10.1039/c6fd00180g.

(8) Zhang, L.; Wahab, O. J.; Jallow, A. A.; O'Dell, Z. J.; Pungsrisai, T.; Sridhar, S.; Vernon, K. L.; Willets, K. A.; Baker, L. A. Recent Developments in Single-Entity Electrochemistry. *Analytical Chemistry*. American Chemical Society May 21, 2024, pp 8036–8055. https://doi.org/10.1021/acs.analchem.4c01406.

(9) Clarke, T. B.; Krushinski, L. E.; Vannoy, K. J.; Colón-Quintana, G.; Roy, K.; Rana, A.; Renault, C.; Hill, M. L.; Dick, J. E. Single Entity Electrocatalysis. *Chemical Reviews*. American Chemical Society August 14, 2024, pp 9015–9080. https://doi.org/10.1021/acs.chemrev.3c00723.

(10) Kim, J. W.; Aruchamy, G.; Kim, B. K. Recent Advances in Single-Entity Electrochemistry for Metal Nanoparticle, Nanodroplet, and Bio-Entity Analysis. *TrAC - Trends in Analytical Chemistry*. Elsevier B.V. December 1, 2023. https://doi.org/10.1016/j.trac.2023.117358.

(11) Ma, H.; Chen, J. F.; Wang, H. F.; Hu, P. J.; Ma, W.; Long, Y. T. Exploring Dynamic Interactions of Single Nanoparticles at Interfaces for Surface-Confined Electrochemical Behavior and Size Measurement. *Nat. Commun.* **2020**, *11* (1). https://doi.org/10.1038/s41467-020-16149-0.

(12) Kang, S.; Nieuwenhuis, A. F.; Mathwig, K.; Mampallil, D.; Lemay, S. G. Electrochemical Single-Molecule Detection in Aqueous Solution Using Self-Aligned Nanogap Transducers. *ACS Nano* **2013**, *7* (12), 10931–10937. https://doi.org/10.1021/nn404440v.

View Article Online
DOI: 10.1039/D6AN00461J

(13) Kim, B. K.; Boika, A.; Kim, J.; Dick, J. E.; Bard, A. J. Characterizing Emulsions by Observation of Single Droplet Collisions - Attoliter Electrochemical Reactors. *J. Am. Chem. Soc.* **2014**, *136* (13), 4849–4852. https://doi.org/10.1021/ja500713w.

(14) Dick, J. E.; Renault, C.; Bard, A. J. Observation of Single-Protein and DNA Macromolecule Collisions on Ultramicroelectrodes. *J. Am. Chem. Soc.* **2015**, *137* (26), 8376–8379. https://doi.org/10.1021/jacs.5b04545.

(15) Oja, S. M.; Robinson, D. A.; Vitti, N. J.; Edwards, M. A.; Liu, Y.; White, H. S.; Zhang, B. Observation of Multipeak Collision Behavior during the Electro-Oxidation of Single Ag Nanoparticles. *J. Am. Chem. Soc.* **2017**, *139* (2), 708–718. https://doi.org/10.1021/jacs.6b11143.

(16) Robinson, D. A.; Liu, Y.; Edwards, M. A.; Vitti, N. J.; Oja, S. M.; Zhang, B.; White, H. S. Collision Dynamics during the Electrooxidation of Individual Silver Nanoparticles. *J. Am. Chem. Soc.* **2017**, *139* (46), 16923–16931. https://doi.org/10.1021/jacs.7b09842.

(17) Banks, C. E.; Davies, T. J.; Evans, R. G.; Hignett, G.; Wain, A. J.; Lawrence, N. S.; Wadhawan, J. D.; Marken, F.; Compton, R. G. Electrochemistry of Immobilised Redox Droplets: Concepts and Applications. *Physical Chemistry Chemical Physics*. October 1, 2003, pp 4053–4069. https://doi.org/10.1039/b307326m.

(18) Ball, J. C.; Marken, F.; Fulian, Q.; Wadhawan, J. D.; Blythe, A. N.; Schröder, U.; Compton, R. G.; Bull, S. D.; Davies, S. G. Voltammetry of Electroactive Oil Droplets. Part II: Comparison of Experimental and Simulation Data for Coupled Ion and Electron Insertion Processes and Evidence for Microscale Convection. *Electroanalysis* **2000**, *12* (13), 1017–1025. https://doi.org/10.1002/1521-4109(200009)12:13<1017::AID-ELAN1017>3.0.CO;2-7.

(19) Donten, M.; Stojek, Z.; Scholz, F. Electron Transfer – Ion Insertion Electrochemistry at an Immobilised Droplet: Probing the Three-Phase Electrode-Reaction Zone with a Pt Disk Microelectrode. *Electrochem. commun.* **2002**, *4* (4), 324–329. https://doi.org/10.1016/S1388-2481(02)00302-8.

(20) Cheng, W.; Compton, R. G. Electrochemical Detection of Nanoparticles by "nano-Impact" Methods. *TrAC - Trends in Analytical Chemistry*. Elsevier B.V. 2014, pp 79–89. https://doi.org/10.1016/j.trac.2014.01.008.

(21) Choi, Y.; Park, C.; Kang, Y.; Muya, J. T.; Jang, D. P.; Chang, J. Temporally Resolved Electrochemical Interrogation for Stochastic Collision Dynamics of Electrogenerated Single Polybromide Droplets. *Anal. Chem.* **2021**, *93* (23), 8336–8344. https://doi.org/10.1021/acs.analchem.1c01366.

(22) Deng, Z.; Elattar, R.; Maroun, F.; Renault, C. In Situ Measurement of the Size Distribution and Concentration of Insulating Particles by Electrochemical Collision on

View Article Online
DOI: 10.1039/D6AN00461J

Hemispherical Ultramicroelectrodes. *Anal. Chem.* **2018**, *90* (21), 12923–12929. https://doi.org/10.1021/acs.analchem.8b03550.

(23) Zhao, W.; Chen, H. Y.; Xu, J. J. Electrogenerated Chemiluminescence Detection of Single Entities. *Chemical Science*. Royal Society of Chemistry April 28, 2021, pp 5720–5736. https://doi.org/10.1039/d0sc07085h.

(24) Krushinski, L. E.; Dick, J. E. Direct Electrochemical Evidence Suggests That Aqueous Microdroplets Spontaneously Produce Hydrogen Peroxide. *Proc. Natl. Acad. Sci. U. S. A.* **2024**, *121* (12). https://doi.org/10.1073/pnas.2321064121.

(25) Layman, B. R.; Dick, J. E. Through-Space Electrochemiluminescence Reveals Bubble Forces at Remote Phase Boundaries. *J. Am. Chem. Soc.* **2024**, *146* (1), 707–713. https://doi.org/10.1021/jacs.3c10505.

(26) Krushinski, L. E.; Herchenbach, P. J.; Dick, J. E. The Gas|liquid Interface Eclipses the Liquid|liquid Interface for Glucose Oxidase Rate Acceleration in Microdroplets. *Proc. Natl. Acad. Sci. U. S. A.* **2024**, *121* (51). https://doi.org/10.1073/pnas.2416353121.

(27) Chamberlayne, C. F.; Zare, R. N. Microdroplets Can Act as Electrochemical Cells. *Journal of Chemical Physics* **2022**, *156* (5). https://doi.org/10.1063/5.0078281.

(28) Ahmed, J. U.; Lutkenhaus, J. A.; Alam, M. S.; Marshall, I.; Paul, D. K.; Alvarez, J. C. Dynamics of Collisions and Adsorption in the Stochastic Electrochemistry of Emulsion Microdroplets. *Anal. Chem.* **2021**, *93* (22), 7993–8001. https://doi.org/10.1021/acs.analchem.1c01027.

(29) Heindel, J. P.; LaCour, R. A.; Head-Gordon, T. The Role of Charge in Microdroplet Redox Chemistry. *Nature Communications* **2024**, *15* (1). https://doi.org/10.1038/s41467-024-47879-0.

(30) German, S. R.; Edwards, M. A.; Chen, Q.; Liu, Y.; Luo, L.; White, H. S. Electrochemistry of Single Nanobubbles. Estimating the Critical Size of Bubble-Forming Nuclei for Gas-Evolving Electrode Reactions. *Faraday Discuss.* **2016**, *193*, 223–240. https://doi.org/10.1039/c6fd00099a.

(31) Lu, S. M.; Chen, J. F.; Peng, Y. Y.; Ma, W.; Ma, H.; Wang, H. F.; Hu, P.; Long, Y. T. Understanding the Dynamic Potential Distribution at the Electrode Interface by Stochastic Collision Electrochemistry. *J. Am. Chem. Soc.* **2021**, *143* (32), 12428–12432. https://doi.org/10.1021/jacs.1c02588.

(32) Vannoy, K. J.; Renault, C.; Dick, J. E. The Microelectrode Insulator Influences Water Nanodroplet Collisions. *Anal. Chem.* **2023**, *95* (18), 7286–7293. https://doi.org/10.1021/acs.analchem.3c00287.

View Article Online
DOI: 10.1039/D6AN00461J

(33) Edwards, M. A.; White, H. S.; Ren, H. Voltammetric Determination of the Stochastic Formation Rate and Geometry of Individual H2, N2, and O2 Bubble Nuclei. *ACS Nano* **2019**, *13* (6), 6330–6340. https://doi.org/10.1021/acsnano.9b01015.

(34) Lu, S. M.; Vannoy, K. J.; Dick, J. E.; Long, Y. T. Multiphase Chemistry under Nanoconfinement: An Electrochemical Perspective. *Journal of the American Chemical Society*. American Chemical Society November 22, 2023, pp 25043–25055. https://doi.org/10.1021/jacs.3c07374.

(35) Defnet, P. A.; Anderson, T. J.; Zhang, B. Stochastic Collision Electrochemistry of Single Silver Nanoparticles. *Curr. Opin. Electrochem.* **2020**, *22*, 129–135. https://doi.org/10.1016/j.coelec.2020.06.004.

(36) Krushinski, L. E.; Qiu, L.; Dick, J. E. Levitating Droplet Electroanalysis. *Anal. Chem.* **2023**. https://doi.org/10.1021/acs.analchem.3c04123.

(37) Chen, X.; Ding, Q.; Bi, C.; Ruan, J.; Yang, S. Lossless Enrichment of Trace Analytes in Levitating Droplets for Multiphase and Multiplex Detection. *Nat. Commun.* **2022**, *13* (1). https://doi.org/10.1038/s41467-022-35495-9.

(38) Salm, E.; Guevara, C. D.; Dak, P.; Dorvel, B. R.; Reddy, B.; Alam, M. A.; Bashir, R. Ultralocalized Thermal Reactions in Subnanoliter Droplets-in-Air. *Proc. Natl. Acad. Sci. U. S. A.* **2013**, *110* (9), 3310–3315. https://doi.org/10.1073/pnas.1219639110.

(39) Xia, Y.; Xu, J.; Li, J.; Chen, B.; Dai, Y.; Zare, R. N. Visualization of the Charging of Water Droplets Sprayed into Air. *Journal of Physical Chemistry A* **2024**, *128* (28), 5684–5690. https://doi.org/10.1021/acs.jpca.4c02981.

(40) Crawford, E. A.; Esen, C.; Volmer, D. A. Real Time Monitoring of Containerless Microreactions in Acoustically Levitated Droplets via Ambient Ionization Mass Spectrometry. *Anal. Chem.* **2016**, *88* (17), 8396–8403. https://doi.org/10.1021/acs.analchem.6b01519.

(41) Qiu, L.; Li, X.; Holden, D. T.; Cooks, R. G. Reaction Acceleration at the Surface of a Levitated Droplet by Vapor Dosing from a Partner Droplet. *Chem. Sci.* **2024**, *15* (31), 12277–12283. https://doi.org/10.1039/d4sc03528c.

(42) Petersson, M.; Nilsson, J.; Wallman, L.; Laurell, T.; Johansson, J.; Nilsson, S. Sample Enrichment in a Single Levitated Droplet for Capillary Electrophoresis. *J. Chromatogr. B Biomed. Sci. Appl.* **1998**, *714* (1), 39–46. https://doi.org/10.1016/S0378-4347(98)00092-9.

(43) Dak, P.; Ebrahimi, A.; Swaminathan, V.; Duarte-Guevara, C.; Bashir, R.; Alam, M. A. Droplet-Based Biosensing for Lab-on-a-Chip, Open Microfluidics Platforms. *Biosensors*. MDPI 2016. https://doi.org/10.3390/bios6020014.

View Article Online
DOI: 10.1039/D6AN00461J

(44) Ebrahimi, A.; Csonka, L. N.; Alam, M. A. Analyzing Thermal Stability of Cell Membrane of Salmonella Using Time-Multiplexed Impedance Sensing. *Biophys. J.* **2018**, *114* (3), 609–618. https://doi.org/10.1016/j.bpj.2017.10.032.

(45) Swaminathan, V. V.; Dak, P.; Reddy, B.; Salm, E.; Duarte-Guevara, C.; Zhong, Y.; Fischer, A.; Liu, Y. S.; Alam, M. A.; Bashir, R. Electronic Desalting for Controlling the Ionic Environment in Droplet-Based Biosensing Platforms. *Appl. Phys. Lett.* **2015**, *106* (5). https://doi.org/10.1063/1.4907351.

(46) Dak, P.; Ebrahimi, A.; Alam, M. A. Non-Faradaic Impedance Characterization of an Evaporating Droplet for Microfluidic and Biosensing Applications. *Lab Chip* **2014**, *14* (14), 2469–2479. https://doi.org/10.1039/c4lc00193a.

(47) Ebrahimi, A.; Dak, P.; Salm, E.; Dash, S.; Garimella, S. V.; Bashir, R.; Alam, M. A. Nanotextured Superhydrophobic Electrodes Enable Detection of Attomolar-Scale DNA Concentration within a Droplet by Non-Faradaic Impedance Spectroscopy. *Lab Chip* **2013**, *13* (21), 4248–4256. https://doi.org/10.1039/c3lc50517k.

(48) Ebrahimi, A.; Alam, M. A. Time-Resolved PCA of "droplet impedance" Identifies DNA Hybridization at NM Concentration. *Sens. Actuators B Chem.* **2015**, *215*, 215–224. https://doi.org/10.1016/j.snb.2015.03.049.

(49) Mavré, F.; Anand, R. K.; Laws, D. R.; Chow, K. F.; Chang, B. Y.; Crooks, J. A.; Crooks, R. M. Bipolar Electrodes: A Useful Tool for Concentration, Separation, and Detection of Analytes in Microelectrochemical Systems. *Anal. Chem.* **2010**, *82* (21), 8766–8774. https://doi.org/10.1021/ac101262v.

(50) Li, M.; Anand, R. K. Recent Advancements in Ion Concentration Polarization. *Analyst*. Royal Society of Chemistry June 21, 2016, pp 3496–3510. https://doi.org/10.1039/c6an00194g.

(51) Li, M.; Anand, R. K. Integration of Marker-Free Selection of Single Cells at a Wireless Electrode Array with Parallel Fluidic Isolation and Electrical Lysis. *Chem. Sci.* **2019**, *10* (5), 1506–1513. https://doi.org/10.1039/c8sc04804e.

(52) Anand, R. K.; Johnson, E. S.; Chiu, D. T. Negative Dielectrophoretic Capture and Repulsion of Single Cells at a Bipolar Electrode: The Impact of Faradaic Ion Enrichment and Depletion. *J. Am. Chem. Soc.* **2015**, *137* (2), 776–783. https://doi.org/10.1021/ja5102689.

(53) Devasinghe, S. U.; Claus, E. L.; Strait, M. E.; Pagariya, D.; Anand, R. K. Electrokinetic Preconcentration and Label-Free Electrical Detection of SARS-CoV-2 RNA at a Packed Bed of Bioconjugated Microspheres. *ACS Sens.* **2024**, *9* (11), 5776–5781. https://doi.org/10.1021/acssensors.4c00427.

View Article Online
DOI: 10.1039/D6AN00461J

(54) Clark, M. J.; Moser, H. J.; Anand, R. K. Dielectrophoretic Capture and Electrochemical Enzyme-Linked Immunosorbent Assay of Single Melanoma Cells at an Array of Interlocked Spiral Bipolar Electrodes. *ChemElectroChem* **2024**, *11* (15). https://doi.org/10.1002/celc.202400182.

(55) Sun, A. C.; Steyer, D. J.; Allen, A. R.; Payne, E. M.; Kennedy, R. T.; Stephenson, C. R. J. A Droplet Microfluidic Platform for High-Throughput Photochemical Reaction Discovery. *Nat. Commun.* **2020**, *11* (1). https://doi.org/10.1038/s41467-020-19926-z.

(56) Dawod, M.; Arvin, N. E.; Kennedy, R. T. Recent Advances in Protein Analysis by Capillary and Microchip Electrophoresis. *Analyst*. Royal Society of Chemistry June 7, 2017, pp 1847–1866. https://doi.org/10.1039/c7an00198c.

(57) Anderson, B. G.; Popov, P.; Cicali, A. R.; Nwamba, A.; Evans, C. R.; Kennedy, R. T. In-Depth Chemical Analysis of the Brain Extracellular Space Using In Vivo Microdialysis with Liquid Chromatography-Tandem Mass Spectrometry. *Anal. Chem.* **2024**, *96* (41), 16387–16396. https://doi.org/10.1021/acs.analchem.4c03806.

(58) Payne, E. M.; Taraji, M.; Murray, B. E.; Holland-Moritz, D. A.; Moore, J. C.; Haddad, P. R.; Kennedy, R. T. Evaluation of Analyte Transfer between Microfluidic Droplets by Mass Spectrometry. *Anal. Chem.* **2023**, *95* (10), 4662–4670. https://doi.org/10.1021/acs.analchem.2c04985.

(59) Koons, J. F.; Cullom, S. C.; Dick, J. E. Microdroplet-Confined Oxygen Reduction Forms Highly Active Transition Metal Alloy Hydroxides at Low Overpotentials for Oxygen Evolution. *J. Mater. Chem. A Mater.* **2025**. https://doi.org/10.1039/d5ta05555e.

(60) Layman, B. R.; Hill, M. L.; Carrel, D. M.; Nguyen, J. H.; Dick, J. E. Exploring the Mechanism of Microdroplet Explosion on an Electrified Interface. *J. Am. Chem. Soc.* **2026**. https://doi.org/10.1021/jacs.5c18741.

(61) Wagner, A. A.; Herrera, D. P.; Rudder, A. L.; Kinsey, C.; Foley, D. A.; Thompson, D. H.; Payne, E. M.; Dick, J. E. Accessing Robust Vaccine Coformulation Stability by Single Adjuvant Detection on a Microelectrode. *Proc. Natl. Acad. Sci. U. S. A.* **2025**, *122* (44). https://doi.org/10.1073/pnas.2522044122.

(62) Glasscott, M. W.; Pendergast, A. D.; Goines, S.; Bishop, A. R.; Hoang, A. T.; Renault, C.; Dick, J. E. Electrosynthesis of High-Entropy Metallic Glass Nanoparticles for Designer, Multi-Functional Electrocatalysis. *Nat. Commun.* **2019**, *10* (1). https://doi.org/10.1038/s41467-019-10303-z.

(63) Colón-Quintana, G. S.; Clarke, T. B.; Dick, J. E. Interfacial Solute Flux Promotes Emulsification at the Water|oil Interface. *Nat. Commun.* **2023**, *14* (1). https://doi.org/10.1038/s41467-023-35964-9.

View Article Online
DOI: 10.1039/D6AN00461J

(64) Ailawar, S. A.; Colón-Quintana, G.; Clarke, T. B.; Dick, J. E. Hydrazine Oxidation on a Single Electrocatalytic Nanoring. *Analyst* **2025**, *151* (2), 458–465. https://doi.org/10.1039/d5an00651a.

(65) Paul, S.; Koons, J. F.; Harrigan, M. L.; Roy, K.; Dick, J. E. Tuning Nanoparticle Microstructure through Nanodroplet-Mediated Electrodeposition: Applications to PtCu Alloy Nanoparticle Synthesis and Electrocatalysis. *Electroanalysis* **2025**, *37* (4). https://doi.org/10.1002/elan.12043.

(66) Rana, A.; Renault, C.; Dick, J. E. Understanding Dynamic Voltammetry in a Dissolving Microdroplet. *Analyst* **2024**, *149* (15), 3939–3950. https://doi.org/10.1039/d4an00299g.

(67) Rana, A.; Nguyen, J. H.; Renault, C.; Dick, J. E. Concentration Enrichment in a Dissolving Microdroplet: Accessing Sub-Nanomolar Electroanalysis. *Anal. Chem.* **2024**, *96* (14), 5384–5391. https://doi.org/10.1021/acs.analchem.3c04971.

(68) Nguyen, J. H.; Rana, A.; Dick, J. E. Amplifying the Electrochemical Footprint of <1000 Molecules in a Dissolving Microdroplet. *Analyst* **2024**, *149* (16), 4222–4229. https://doi.org/10.1039/d4an00504j.

(69) Rana, A.; Renault, C.; Dick, J. E. Measuring Liquid-into-Liquid Diffusion Coefficients by Dissolving Microdroplet Electroanalysis. *Anal. Chem.* **2023**, *95* (51), 18748–18753. https://doi.org/10.1021/acs.analchem.3c03256.

(70) Rana, A.; Clarke, T. B.; Nguyen, J. H.; Dick, J. E. Adsorbed Microdroplets Are Mobile at the Nanoscale. *Proc. Natl. Acad. Sci. U. S. A.* **2024**, *121* (47). https://doi.org/10.1073/pnas.2412148121.

(71) Wallace, B. J.; Makhnun, M.; Bachnak, R.; Kim, P.; Ahmed, M.; Dutcher, C. S.; Wilson, K. R.; Ajoy, A. Enhanced Reactivity at the Oil-Water Interface Accelerates the Synthesis of Zymonic Acid in Microemulsions. *Chem. Sci.* **2025**, *16* (33), 15155–15165. https://doi.org/10.1039/d5sc03258j.

(72) Kumar, A.; Mondal, S.; Banerjee, S. Aqueous Microdroplets Capture Elusive Carbocations. *J. Am. Chem. Soc.* **2021**, *143* (6), 2459–2463. https://doi.org/10.1021/jacs.0c12512.

(73) Chen, X.; Xia, Y.; Yang, Y.; Xu, Y.; Jia, X.; Zare, R. N.; Wang, F. Microdroplet-Mediated Multiphase Cycling in a Cloud of Water Drives Chemoselective Electrolysis. *J. Am. Chem. Soc.* **2024**, *146* (43), 29742–29750. https://doi.org/10.1021/jacs.4c11224.

(74) Song, X.; Xu, J.; Sun, C.; Lyu, L.; Kui, H.; Zhang, R.; Abliz, Z.; Zare, R. N. Dark Reactions in Microdroplets Explain Widespread Artifacts in Metabolomic Profiling. *ACS Measurement Science Au* **2026**. https://doi.org/10.1021/acsmeasuresciau.5c00146.

View Article Online
DOI: 10.1039/D6AN00461J

(75) Picknett, R. G.; Bexon, R. The Evaporation of Sessile or Pendant Drops in Still Air. *J. Colloid Interface Sci.* **1977**, *61* (2).

(76) Dietrich, E.; Kooij, E. S.; Zhang, X.; Zandvliet, H. J. W.; Lohse, D. Stick-Jump Mode in Surface Droplet Dissolution. *Langmuir* **2015**, *31* (16), 4696–4703. https://doi.org/10.1021/acs.langmuir.5b00653.

(77) Encarnación Escobar, J. M.; Dietrich, E.; Arscott, S.; Zandvliet, H. J. W.; Zhang, X.; Lohse, D. Zipping-Depinning: Dissolution of Droplets on Micropatterned Concentric Rings. *Langmuir* **2018**, *34* (19), 5396–5402. https://doi.org/10.1021/acs.langmuir.8b00256.

(78) Xu, W.; Leeladhar, R.; Kang, Y. T.; Choi, C. H. Evaporation Kinetics of Sessile Water Droplets on Micropillared Superhydrophobic Surfaces. *Langmuir* **2013**, *29* (20), 6032–6041. https://doi.org/10.1021/la400452e.

(79) Erbil, H. Y.; McHale, G.; Newton, M. I. Drop Evaporation on Solid Surfaces: Constant Contact Angle Mode. *Langmuir* **2002**, *18* (7), 2636–2641. https://doi.org/10.1021/la011470p.

(80) Han, P.; Yang, L. jun; Zhu, Z.; Liang, X.; Wu, W. Suppression of Coffee-Ring Effect in Droplets with Varying Particle Concentrations Induced by Laser. *ACS Omega* **2025**, *10* (32), 35785–35792. https://doi.org/10.1021/acsomega.5c02579.

(81) Dick, J. E.; Rana, A.; Renault, C. System and Method for Measuring Electrochemistry of Dynamically Dissolving Droplets. US 12,517,083 B2, March 19, 2024.

(82) Hamada, M.; de Anna, P. A Method to Measure the Diffusion Coefficient in Liquids. *Transp. Porous Media* **2023**, *146* (1–2), 463–474. https://doi.org/10.1007/s11242-021-01704-0.

(83) Department of Environmental Toxicology. *Intermedia Transfer Factors for Contaminants Found at Hazardous Waste Sites 1,2 DICHLOROETHANE (DCA)*; 1994. https://dtsc.ca.gov/wp-content/uploads/sites/31/2018/01/12dca.pdf

(84) Zeng, B.; Wang, Y.; Diddens, C.; Zandvliet, H. J. W.; Lohse, D. Droplet Dissolution Driven by Emerging Thermal Gradients and Marangoni Flow. *Phys. Rev. Fluids* **2022**, *7* (6). https://doi.org/10.1103/PhysRevFluids.7.064006.

(85) Popov, Y. O. Evaporative Deposition Patterns: Spatial Dimensions of the Deposit. *Phys. Rev. E Stat. Nonlin. Soft Matter Phys.* **2005**, *71* (3). https://doi.org/10.1103/PhysRevE.71.036313.

(86) Chong, K. L.; Li, Y.; Ng, C. S.; Verzicco, R.; Lohse, D. Convection-Dominated Dissolution for Single and Multiple Immersed Sessile Droplets. *J. Fluid Mech.* **2020**, *892*. https://doi.org/10.1017/jfm.2020.175.

View Article Online
DOI: 10.1039/D6AN00461J

(87) Boyle, R. *The Sceptical Chymist*; London, J.M. Dent & Sons, ltd.; New York, E.P. Dutton & Co, 1911.

(88) Deegan, R.; Bakajin, O.; Dupont, T.; Huber, G.; Nagel, S.; Witten, T. Capillary Flow as the Cause of Ring Stains from Dried Liquid Drops. *Nature* **1997**, *389*, 827–829. https://doi.org/https://doi.org/10.1038/39827.

(89) Zhang, H.; Oellers, T.; Feng, W.; Abdulazim, T.; Saw, E. N.; Ludwig, A.; Levkin, P. A.; Plumeré, N. High-Density Droplet Microarray of Individually Addressable Electrochemical Cells. *Anal. Chem.* **2017**, *89* (11), 5832–5839. https://doi.org/10.1021/acs.analchem.7b00008.

(90) Nguyen, J. H.; Rana, A.; Hatch, S. M.; Dick, J. E. Dissolving Microdroplet Electroanalysis Enables Attomolar-Level Detection. *Analyst* **2025**, *150* (19), 4285–4292. https://doi.org/10.1039/d5an00795j.

View Article Online
DOI: 10.1039/D6AN00461J

This Perspective does not include new experimental or computational data. All data discussed are from previously published studies, and relevant sources are cited throughout the article. No supplementary information is associated with this work.